

METHODS

Chemistry and photochromism

7-aminonitrazepam (**2**)^{1,2} and the nitroso derivatives **1a**³, **1b**⁴, **1c**⁵, and **1d**⁶ were synthesized according to reported procedures. Commercial reagents and starting materials were purchased from Acros Organics, Alfa-Aesar, Fisher Scientific, Sigma Aldrich or VWR and used without any further purification. Solvents were used in p.a. quality and dried according to common procedures, if necessary. Commercially phosphate buffer (pH = 7.4) was used for investigations of the photochromic properties. Dry nitrogen was used as inert gas atmosphere. A Biotage Isolera flash purification system with UV/Vis detector using Sigma Aldrich MN silica gel 60 M (40-63 μm , 230-400 mesh) for normal phase or pre-packed Biotage SNAP cartridges (KP C18 HS) for reversed phase chromatography was used for automated flash column chromatography. Reaction monitoring via TLC and determination of R_f values was accomplished on alumina plates coated with silica gel (Merck silica gel 60 F254, 0.2 mm). Melting points were measured with a Stanford Research Systems OptiMelt MPA 100 device and are uncorrected. NMR spectra were measured on BrukerAvance 300 (¹H 300.13 MHz, ¹³C 75.48 MHz), BrukerAvance 400 (¹H 400.13 MHz, ¹³C 100.61 MHz) and BrukerAvance III 600 (¹H 600.25 MHz, ¹³C 150.95 MHz) instruments. The spectra are referenced against the NMR-solvent (DMSO-*d*₆: $\delta\text{H} = 2.50$ ppm) and the chemical shifts δ are reported in ppm. Resonance multiplicity is abbreviated as: s (singlet), d (doublet), t (triplet), q (quartet), m (multiplet) and b (broad). Carbon NMR signals are reported using DEPT135 and ¹H-¹³C HSQC spectra with (+) for primary/tertiary, (-) for secondary and (q) for quaternary carbons. An Agilent Q-TOF 6540 UHD (ESI-MS) instrument was used for recording mass spectra. UV/Vis absorption spectroscopy was accomplished using a Varian Cary Bio 50 UV/Vis spectrometer in 10 mm quartz cuvettes. IR-spectra were recorded on an Agilent Cary 630 FT-IR spectrometer and the peak positions are reported in wavenumbers (cm^{-1}). Analytical HPLC measurements were performed on an Agilent 1220 Infinity LC (column: Phenomenex Luna 3 μM C18(2) 100 \AA , 150 x 2.00 mm; flow: 0.3 mL/min at 30 °C; solvent A: MilliQ water with 0.05% vol TFA; solvent B: MeCN). The ratios at the photostationary states (PSSs) were determined by HPLC measurements with a detection wavelength at the isosbestic point. For determination of the thermal half-lives the solutions were irradiated until the photostationary state was reached. Then the solutions were left at 25 °C and the recovery of the absorbance of the *trans*-isomer at λ_{max} was measured. Consequently, the thermal half-life was calculated by fitting the data with a single exponential function. An Agilent 1260 system (column: Phenomenex Luna 10 μM C18(2) 100 \AA , 250 x 21.2 mm; flow: 22.0 mL/min; solvent A: MilliQ water with 0.05% vol TFA; solvent B: MeCN) was used for preparative HPLC purification. Light sources for illumination were: $\lambda = 365$ nm (Herolab hand-held lamp UV-6 L, 6 W), $\lambda = 455$ nm (OSRAM Oslon SSL 80 LED, 700 mA, 1.12 W), and $\lambda = 530$ nm (CREE-XP green, 700 mA, 3.7 W). The power of the light is given based on the specifications supplied by the company when the lamps were purchased. Final compounds for biological testing possess a purity $\geq 95\%$ determined by HPLC measurements with detection at 220 nm and 254 nm.

(E)-7-((1H-pyrazol-4-yl)diazenyl)-5-phenyl-1,3-dihydro-2H-benzo[e][1,4]diazepin-2-one (3a)

4-Nitroso-1H-pyrazole (**1a**, 71 mg, 0.73 mmol, 1.2 eq.) was added to a solution of amino-benzodiazepine (**2**, 153 mg, 0.61 mmol, 1.0 eq.) in glacial acetic acid (8 mL). Then the mixture was stirred 3 days at room temperature, quenched by adding a saturated aqueous solution of NaHCO₃ (30 mL) and diluted with EtOAc (30 mL). After separation of the layers, the aqueous layer was extracted with EtOAc (3x20 mL). The combined organic layers were dried over Na₂SO₄, filtered and the solvent was removed under reduced pressure. Purification by preparative HPLC (15% - 45% MeCN in 25min, t_R = 18.8 min) afforded the desired product (30 mg, 15%) as yellow solid. R_f 0.55 (CH₂Cl₂/MeOH 9:1); m.p. 133 °C; ¹H-NMR (600 MHz, DMSO-*d*₆) δ = 13.21 (bs, 1H), 10.86 (s, 1H), 8.22 (bs, 2H), 7.98 (dd, *J* = 8.7, 2.3 Hz, 1H), 7.56 (d, *J* = 2.3 Hz, 1H), 7.55 – 7.51 (m, 3H), 7.48 – 7.43 (m, 2H), 7.39 (d, *J* = 8.8 Hz, 1H), 4.21 (s, 2H); ¹³C-NMR (151 MHz, DMSO-*d*₆) δ = 170.0 (q), 169.7 (q), 158.1 (+), 157.9 (+), 146.7 (q), 141.2 (q), 140.8 (q), 138.6 (q), 130.6 (+), 129.4 (+), 128.4 (+), 126.4 (q), 125.0 (+), 124.4 (+), 122.2 (+), 56.9 (-); IR (neat) ν = 3138, 2866, 1707, 1674, 1614, 1487, 1439, 1394, 1346, 1200, 1133, 995, 839, 798, 723 cm⁻¹; HRMS (ESI) calculated. for C₁₈H₁₅N₆O (M+H)⁺ m/z = 331.1302; found 331.1303.

(E)-4-((2-Oxo-5-phenyl-2,3-dihydro-1H-benzo[e][1,4]diazepin-7-yl)diazenyl)benzenesulfonic acid (9) (3b)

A 1:1 mixture of tetrabutylammonium 4-nitrosobenzenesulfonate (**1b**) and its corresponding nitro derivative (236 mg, 0.54 mmol, 1.0 eq. of nitroso compound) was added to a solution of amino benzodiazepine (**2**, 68 mg, 0.27 mmol, 1.0 eq.) in acetic acid (2 mL) and CH₂Cl₂ (1 mL). After stirring the mixture for 24 h at room temperature the solvent was removed *in vacuo*. Purification by automated flash column chromatography (CH₂Cl₂/MeOH, 3% - 25% MeOH) and subsequent preparative HPLC (2% - 65% MeCN in 10 min, t_R = 7.2 min) yielded **3b** (69 mg, 61%) as yellow solid. R_f 0.03 (CH₂Cl₂/MeOH 9:1); m.p. 280 °C (decomposition); ¹H-NMR (600 MHz, DMSO-*d*₆) δ = 11.32 (s, 1H), 8.23 (dd, *J* = 8.8, 2.4 Hz, 1H), 7.81 – 7.78 (m, 2H), 7.77 – 7.73 (m, 3H), 7.68 (t, *J* = 7.4 Hz, 1H), 7.64 (dd, *J* = 8.3, 1.3 Hz, 2H), 7.57 (t, *J* = 7.7 Hz, 2H), 7.52 (d, *J* = 8.9 Hz, 1H), 4.34 (s, 2H); ¹³C-NMR (151 MHz, DMSO-*d*₆) δ = 172.5 (q), 168.9 (q), 151.4 (q), 151.1 (q), 146.5 (q), 143.0 (q), 135.8 (q), 132.5 (+), 130.7 (+), 128.8 (+), 128.6 (+), 126.8 (+), 126.2 (+), 124.4 (q), 122.9 (+), 122.2 (+), 54.6 (-); IR (neat) ν = 3489, 3135, 2930, 1715, 1614, 1484, 1435, 1387, 1342, 1230, 1163, 1115, 1029, 1006, 846, 742, 697 cm⁻¹; HRMS (ESI) calculated. for C₂₂H₁₆N₄O₄S (M+H)⁺ m/z = 421.0965; found 421.0964.

(E)-4-((2-Oxo-5-phenyl-2,3-dihydro-1H-benzo[e][1,4]diazepin-7-yl)diazenyl)benzene-sulfonamide (3c)

Freshly prepared 4-nitrosobenzenesulfonamide (**3c**, 238 mg, 1.38 mmol, 3.0 eq.) was added to a solution of amino benzodiazepine trifluoroacetate salt (168 mg, 0.46 mmol, 1.0 eq.) in CH₂Cl₂ (6 mL) and acetic acid (2 mL). After stirring the mixture for 24 h at 40 °C the solvent was removed *in vacuo*. The residue was purified by automated flash column chromatography (CH₂Cl₂/MeOH, 3% - 10% MeOH) yielding **3c** (140 mg, 73%) as orange solid. Material for analytical characterization as well as for biological testing was further purified by preparative HPLC (10% - 75% MeCN in 18 min, t_R = 11.1 min).

R_f 0.14 (CH₂Cl₂/MeOH 97:3); m.p. 207 °C; ¹H-NMR (400 MHz, DMSO-*d*₆) δ = 11.08 (s, 1H), 8.16 (dd, *J* = 8.8, 2.3 Hz, 1H), 7.98 (s, 4H), 7.79 (d, *J* = 2.3 Hz, 1H), 7.58 – 7.46 (m, 8H), 4.27 (s, 2H); ¹³C-NMR (101 MHz, DMSO-*d*₆) δ = 170.1 (q), 169.8 (q), 153.2 (q), 146.2 (q), 146.0 (q), 143.0 (q), 138.0 (q), 131.1 (q), 129.7 (+), 128.5 (+), 127.8 (+), 127.1 (+), 126.1 (q), 124.9 (+), 123.0 (+), 122.6 (+), 56.5 (-); IR (neat) ν = 3243, 3071, 1700, 1674, 1610, 1484, 1390, 1334, 1200, 1163, 1014, 902, 842, 798, 746, 697 cm⁻¹; HRMS (ESI) calculated. for C₂₁H₁₈N₅O₃S (M+H)⁺ m/z = 420.1133; found 420.1125.

(*E*)-5-Phenyl-7-(pyridin-2-yl-diazenyl)-1,3-dihydro-2*H*-benzo[*e*][1,4]diazepin-2-one (3d) (Glyght)

2-Nitrosopyridine (**1d**, 108 mg, 1.00 mmol, 2.0 eq.) was added to a solution of amino-benzodiazepine (**2**, 126 mg, 0.50 mmol, 1.0 eq.) in CH₂Cl₂ (3 mL) and acetic acid (1 mL). After stirring the mixture for 24 h at room temperature the solvent was removed *in vacuo*. The residue was purified by automated reversed phase flash column chromatography (MeCN/H₂O with 0.05% TFA, 5% - 100% MeCN) and subsequent preparative HPLC (10% - 60% MeCN in 20 min, t_R = 13.4 min) yielding **Glyght** (125 mg, 73%) as yellow solid. R_f 0.63 (CH₂Cl₂ + 1% Et₃N/MeOH 9:1); m.p. 222 °C; ¹H-NMR (600 MHz, DMSO-*d*₆) δ = 10.98 (s, 1H), 8.67 (ddd, *J* = 4.7, 1.8, 0.8 Hz, 1H), 8.17 (dd, *J* = 8.7, 2.3 Hz, 1H), 8.00 (ddd, *J* = 8.1, 7.4, 1.8 Hz, 1H), 7.79 (d, *J* = 2.2 Hz, 1H), 7.68 (dt, *J* = 8.0, 1.0 Hz, 1H), 7.56 – 7.51 (m, 4H), 7.48 – 7.44 (m, 3H), 4.25 (s, 2H); ¹³C-NMR (151 MHz, DMSO-*d*₆) δ = 170.1 (q), 169.3 (q), 162.6 (q), 149.4 (+), 146.1 (q), 143.0 (q), 138.9 (+), 138.8 (q), 130.5 (+), 129.3 (+), 128.4 (+), 126.8 (+), 126.7 (q), 125.8 (+), 125.1 (+), 122.4 (+), 113.3 (+), 57.2 (-); IR (neat) ν = 3105, 3058, 2930, 2881, 1707, 1610, 1487, 1424, 1327, 1245, 1174, 1111, 936, 846, 790, 753, 701 cm⁻¹; HRMS (ESI) calculated. for C₂₀H₁₆N₅O (M+H)⁺ m/z = 342.1349; found 342.1358.

***In vitro* electrophysiological studies.**

Cell culture and ion channel expression.

In vitro testing of the compound was performed using a line of Chinese hamster ovary (CHO) cells that were transiently transfected with cDNA of different subunits of GABA_A and GlyRs, and 5HT₃ARs. CHO cells were cultured as previously described^{7,8}. Transfection was performed with Lipofectamine 3000 (Life Technology, USA). The following receptor combinations were investigated during this study: $\alpha 1$ zebrafish and $\alpha 2$ zebrafish homomeric GlyRs, $\alpha 1$ human and $\alpha 2$ mouse homomeric GlyRs, $\alpha 1$ human/ β mouse and $\alpha 2$ mouse/ β mouse heteromeric GlyRs; heteromeric GABA_ARs formed by human $\alpha 1/\beta 2/\gamma 2$ subunits. Identification of transfected cells was assured by simultaneous transfection of cDNA of green fluorescent protein (GFP); $\alpha 1$ subunit of GABA_A receptor contained GFP as part of the construct. Electrophysiological recordings were performed in the fluorescent cells 24-72 hours after transfection.

Electrophysiological recordings in cell lines.

Whole-cell patch-clamp recordings were held at room temperature (20-25 °C) using an EPC-9 amplifier (HEKA Elektronik, Germany). Cells were continuously superfused with external solution containing (mM): NaCl 140, CaCl₂ 2, KCl 2.8, MgCl₂ 4, HEPES 20, glucose 10; pH 7.4; 320-330 mOsm. Intracellular solution used for filling recording patch pipettes contained (mM): KCl - 140, MgCl₂ - 2, MgATP - 2, BAPTA (tetrapotassium salt) - 2; pH 7.3 at 20 °C; 290 mOsm. Pipettes were pulled from borosilicate glass capillaries (Harvard Apparatus Ltd, USA) and had resistances of 5-10 MOhm. For the rapid replacement of the solutions, the fast application system was used. Three parallel rectangular tubes (100x100 μ m) were positioned 40-50 μ m above the recorded cell. The movement of the tubes was controlled by a computer-driven fast exchange system (SF 77A Perfusion Fast-Step, Warner, USA) allowing a 10–90% solution exchange in 3–5 ms, as measured by open electrode controls (1/10 external solution/water). Cells with low input resistance (<150 MOhm) and a rapid run-down (>30% with repetitive application) were excluded from analysis. UV illumination was provided by computer-driven 365 nm LED (Thorlabs), positioned 5 cm above the recorded cell, the power of UV light was reaching 0.6 mW/mm² at the level of recording chamber, as determined using an optical power meter (Thorlabs). Electrophysiological recordings were performed with PatchMaster (HEKA Electronic, Germany) software.

Electrophysiological data analysis and statistics

To obtain the concentration/response curves the amplitude of evoked currents was plotted against different concentrations of agonists and Glyght (Figure 5ghi), and fitted using a non-linear fitting routine of the Origin 7.5 software (OriginLabs, USA) with the Hill equation:

$$\text{For glycine: } I = I_{\max}/(1+(EC_{50}/[A])^{n_H})$$

$$\text{For Glyght: } I = I_{\max}/(1+([Glyght]/IC_{50})^{n_H})$$

Where I is the normalized current amplitude induced by the agonist at concentration $[A]$, I_{\max} is a maximal current induced at given cell, n_H is the Hill coefficient, EC_{50} or IC_{50} are the concentrations at which a half-maximum response was induced, and $[Glyght]$ is the concentration of Glyght used in the experiment. Ionic current recordings were analyzed with Igor Pro 6.02 and Origin 9.0 software. For statistical analysis paired and unpaired t-tests were used. Data are represented as means \pm SEM.

Drugs

Commercial drugs were obtained from Sigma-Aldrich (France). Stock solutions of Glycylglycine (10 mM) and picrotoxin (50 mM) were prepared using DMSO and then diluted to the final concentration in extracellular solution. Stock solutions of GABA (1 M), glycine (1 M) and 5HT (10 mM) were prepared using MilliQwater. Non-saturating and saturating concentrations of GABA and glycine were chosen accordingly to the agonist EC₅₀ value for given receptor. Mean GABA EC₅₀ for $\alpha 1/\beta 2/\gamma 2$ GABA_A receptors was determined to be 8 μ M (n = 6); mean glycine EC₅₀ for $\alpha 1Z$ GlyRs was 35 μ M (Supplementary figure 5g, n = 6), for $\alpha 2Z$ 70 μ M (Supplementary figure 5g; n = 6); for $\alpha 1\beta$ – 73 μ M (n = 9), $\alpha 2\beta$ – 130 μ M (n = 9). Thus, non-saturating concentration of GABA was 5 μ M, of glycine – 20 μ M for $\alpha 1$, 50 μ M for $\alpha 2$, 30 μ M for $\alpha 1\beta$ and 100 μ M for $\alpha 2\beta$. Saturating concentration for GABA_A was 300 μ M, for $\alpha 1$ and $\alpha 2$ GlyRs – 300 μ M and 500 μ M of glycine respectively.

Electrophysiology in neuromuscular junction (NMJ)

Diaphragm muscle with the attached phrenic nerve was isolated from mouse and mounted to experimental chamber. Preparation was perfused continuously with an aerated physiological saline solution (mM): NaCl - 125; KCl – 2.5; CaCl₂ – 2; NaH₂PO₄ – 1; MgCl₂ – 1; glucose – 11. The pH of solution was adjusted to 7.3 at 20 °C. To prevent muscle contraction following nerve stimulation, the muscles were transversely dissected 1 hour before experiment. Intracellular recording of end-plate potentials (EPPs) was done with sharp glass microelectrodes (4-9 M Ω) using Axoclamp 900A electrophysiological amplifier (Molecular Devices, CA, USA). The motor nerve was stimulated with electrical pulses of supra-threshold amplitude and 0.1 - 0.2 ms duration with Digitimer DS3 stimulator. EPPs were recorded at low frequency stimulation of motor nerve (0.2 Hz). The resting membrane potential (RMP) of the muscle fiber was monitored through the entire experiment; those experiments that showed significant drop of RMP were not analyzed. Electrophysiological signals were digitized at 5 μ s intervals stored and processed off-line with a PC. For analysis of EPP amplitude dynamics the first signal in recording was taken as 100 percent.

***In vivo* studies**

Animal housing and photoswitchable behavioral assays

Tupfel-Lon *Danio rerio* embryos were raised in darkness for 6 days post fertilization (dpf) in UV filtered tap water in Petri dishes (daily cleaned and refilled) at 28.5 °C. Larvae were recorded and video analyzed using the Zebrabox and Zebralab software (ViewPoint Life Sciences). Briefly, 7 dpf larvae were left undisturbed for 40 minutes in 200 µL fresh UV filtered water and in darkness. Continuously, 100 µL were removed and replaced with a double concentrated treatment solution and data and video recording begun. For the first 20 - 40 minutes, larvae were kept in darkness measuring basal activity, named as the resting period (RP). From the 20th minute, 2 minutes 365 nm and 455 nm light changes were applied for 3 consecutive cycles, assuring the solutions to transit between their respective *cis* and *trans* photostationary states. Illumination periods at specific wavelengths lasted for 2 minutes.

Data analysis and statistics

Zebrafish tracking was performed in real time and data acquisition integrated one- or two-minute intervals using the Zebralab software (ViewPoint Life Science). Data statistical analysis was performed using GraphPad Prism 6 software. Selective illumination was performed with two ordered based [evenly distributed] arrays of 12 light emitting diodes (LEDs) for each wavelength placed 12 cm afar of the multiwell plate. The light intensities, measured with an optical power meter (model Newport 1916-C), were 5.9 W·m⁻² for 365 nm (UV) and 2.4 W·m⁻² for 455 nm (Visible-Blue). Larvae activity was measured as the sum of fast swimming durations over one-minute integration per well (fast swimming time). Distance activity was measured as the sum of swimming distances (in millimeters) during burst activities over one-minute integration. Data were analyzed following Two-way ANOVA (p-value 0.05) and are presented as mean ± standard error of the mean (s.e.m.) with the number of larvae (n) indicated in each case.

UVAR. UV/Visible activity ratio was extracted from raw activity data as the swimming ratio between the total of six minutes of UV illumination and the total of six minutes of visible illumination for each drug treatment.

Modeling studies

Receptor Structures

The structure of the homopentameric wild-type α_1 ZGly receptor (α_1 ZGlyR) used was the cryo-electron microscopy structure solved in the presence of Gly (PDB entry 3JAE, corresponding to an open state⁹). Missing side chains and hydrogen atoms were added using the psfgen plugin (version 1.6.4¹⁰) in VMD¹¹ (version 1.9.2). For α_2 H GlyR we constructed a homology model of the isoform 2B (UniProt code P23416-2) using the α_1 ZGlyR structure as template (sequence identity = 89.2 %). At the ECD/TMD interface, α_2 H GlyR differs by only two residues with respect to α_1 ZGlyR (85-86 VT → IA).

Glyght ligand

The initial structures of the Glyght compound (*cis* and *trans* isomers) were created employing the program Avogadro¹² (version 1.1.1). For each isomer, two 1,4-diazepine ring conformations, M and P, were considered, which differ in orientation (below or above the plane, respectively) of C3 and the phenyl substituent of C5¹³. For canonical benzodiazepines that bind to the classical allosteric site of the GABA_A receptor, the M conformation is the bioactive one¹³ (i.e. the one that shows higher affinity for receptor). However, it is not known a priori whether Glyght would exhibit similar conformational preferences, since here we consider binding to a different receptor (GlyR) and to distinct site(s). All four ligand structures (*cis*/M, *cis*/P, *trans*/M and *trans*/P) were optimized using Density Functional Theory¹⁴ (DFT), with the B3LYP functional¹⁵ and the 6-31++G (d,p) basis set. Calculations were performed with the Gaussian 09 (G09) program package¹⁶. For the *trans* isomer, the two conformers differ only by 0.02 kcal/mol and thus their Boltzmann populations are expected to be very similar (50.8% and 49.2% for P and M, respectively). In other words, the two conformers can be present at room temperature. In the case of the *cis* isomer, the M conformer is significantly more stable (by 1.5 kcal/mol) than the P conformer, and thus it is the predominant conformer (with a Boltzmann population of 92%).

Docking calculations

Autodock Vina¹⁷ (version 1.1.2) was employed for ligand-receptor docking. The maximum energy difference between the best and worst binding modes and the exhaustiveness were set to default values (3kcal/mol and 8, respectively). Instead, the maximum number of modes was increased to 20 in order to increase the docking sampling. This protocol was repeated 10 times, starting with different random seeds, so that a total number of 200 binding modes was obtained for each of the four possible conformers of Glyght (*cis*/M, *cis*/P, *trans*/M and *trans*/P). For the *trans* isomer, the docking poses obtained for the corresponding M and P conformations were grouped together to carry out the analysis (since the two conformers are almost isoenergetic, see above), resulting in a total of 400 docking poses were considered. For the *cis* isomer, the 200 docking poses obtained of each conformer were analyzed separately, and only the most populated conformer, *cis*M, is discussed in the text.

As the location of the putative binding site(s) for Glyght in GlyR is not known, we designed a multilevel binding site screening approach, in the spirit of reference (www.bonvinlab.org/education/HADDOCK-binding-sites/): (1) blind docking using the whole receptor as a search space, (2) information-driven docking focused on the interfacial site between the extracellular and transmembrane domains identified in (1), in order to refine the docking poses and (3) a flexible docking centered in the

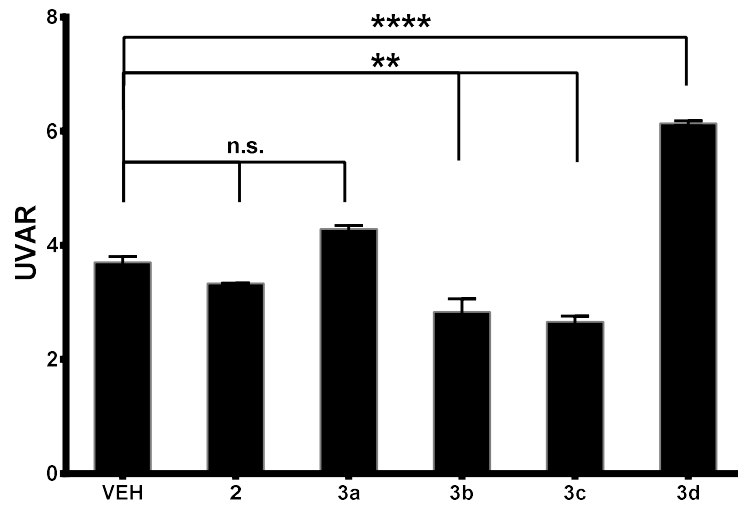
intersubunit site found in (2) in where the residues K292, T71, T70 (in one subunit) and S289, T70, A68, S66, P291, P201, Q202, L290, R75, R234, F161, Y239, E69 and T71 (in the adjacent subunit) were allowed to move and adapt to the ligand poses.

Analysis of the docking results

The initial blind docking results were analyzed in terms of the number density of the ligand poses. Previous studies have successfully used this type of analysis to identify ligand binding sites in other ion channels^{18,19}. The underlying assumption is that regions of continuous density (or high occupancy) should represent regions of tighter binding. The number density value was computed using the Volmap plugin²⁰ of VMD¹¹. Namely, each Glyght position was replaced with a normalized Gaussian distribution of width equal to 1.5 Å and the Gaussians were additively distributed on a three-dimensional grid of dimensions 0.5 x 0.5 x 0.5 Å³. For the information-driven docking, we analyzed the most populated pose clusters using the quality threshold algorithm implemented in VMD (<https://github.com/luisico/clustering>) in order to delineate the specific site within the ECD/TMD interface.(3) The flexible docking results were analyzed in terms of the interactions between the ligand and the receptor. On one hand, statistical analysis of protein residues close to the Glyght docking poses was carried out and the percentage contact frequency was calculated considering that a receptor-ligand contact is present if the protein residue is within 5 Å of Glyght. It is assumed that amino acids with high frequencies pinpoint possible binding residues. On the other hand, the representative structure of the most populated cluster(s) was analyzed using the Binana algorithm²¹. The images of the modelling section were generated with either the UCSF Chimera package²² or the VMD program¹¹.

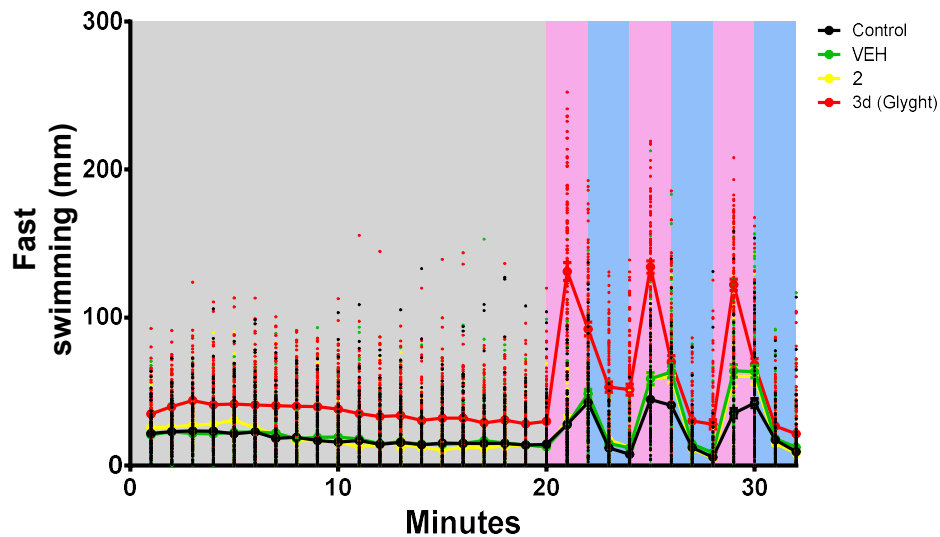
Supplementary Figures

Supplementary Figure 1



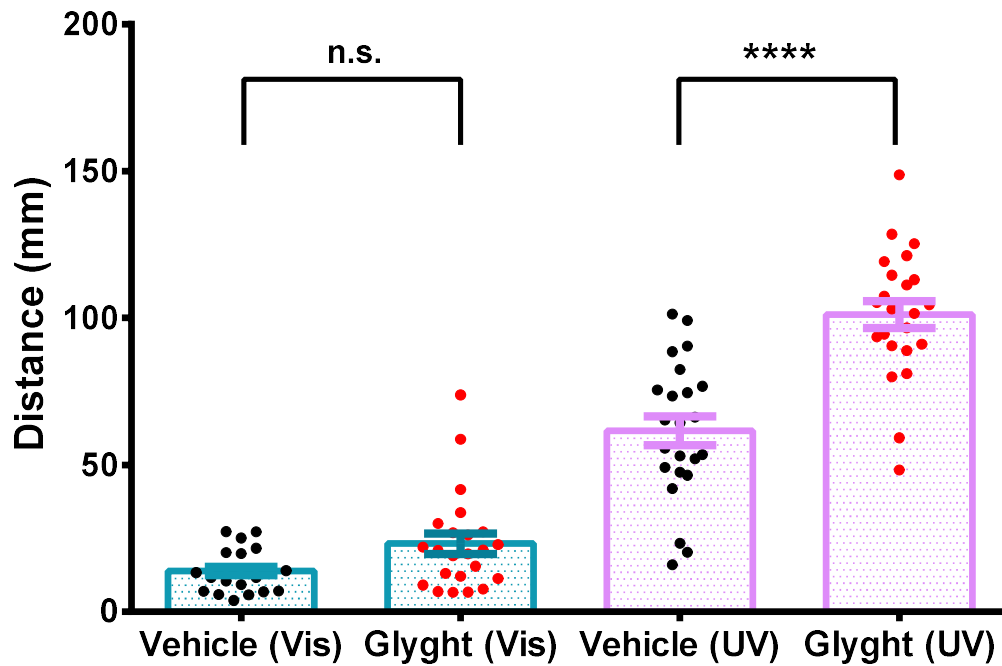
The ratio between activities during UV and visible cycles can be used as a photoswitchable behavior score. The UV/vis activity ratio (UVAR) calculated for each compound can be compared to control UVAR (endogenous photoresponses in vehicle) and provide a simple means to evaluate statistically the significance of the differences. Dunnett's multiple comparison test was conducted (p -value = 0.05). **3b-c** and **3d (Glyght)** were significantly different from vehicle (VEH) with p -values $**p < 0.01$ and $****p < 0.0001$, respectively. In independent experiments, an UVAR = 3.7 ± 0.18 was consistently found in vehicle-treated 7 dpf Tupfel-Lon zebrafish in the described experimental conditions.

Supplementary Figure 2



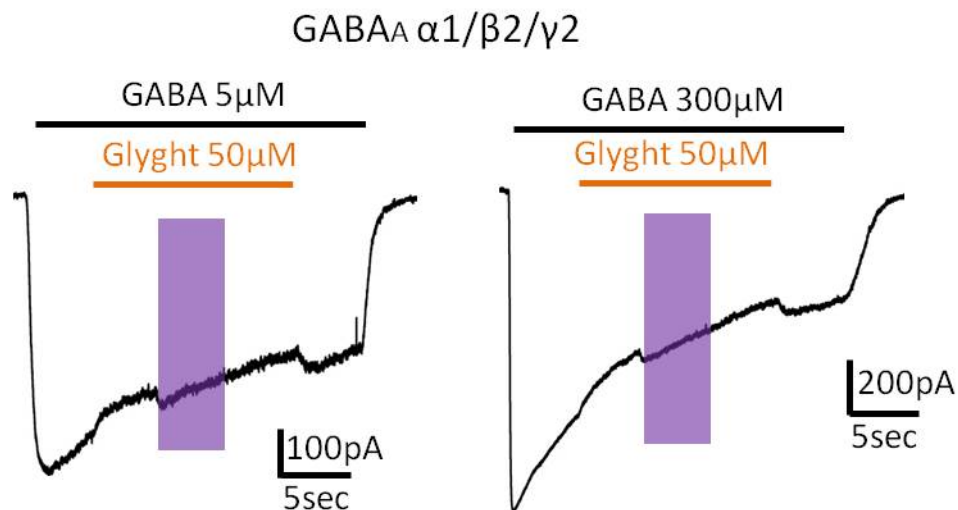
Larvae fast movements activities were analyzed every minute ($\text{mm} \cdot \text{min}^{-1}$) in five independent experiments –Control (larvae clean water, $n = 111$), VEH (1%DMSO, $n = 95$), **2** ($n = 46$) and **3d** (Glyght) ($n = 94$),. Experiments record larvae burst depending activity for 20 minutes in Dark condition (RP) followed by 3 consecutive cycles of 2 minutes 365 nm and 455 nm light exposures. Error bars represent S.E.M. for treated larvae over one-minute integration periods.

Supplementary Figure 3



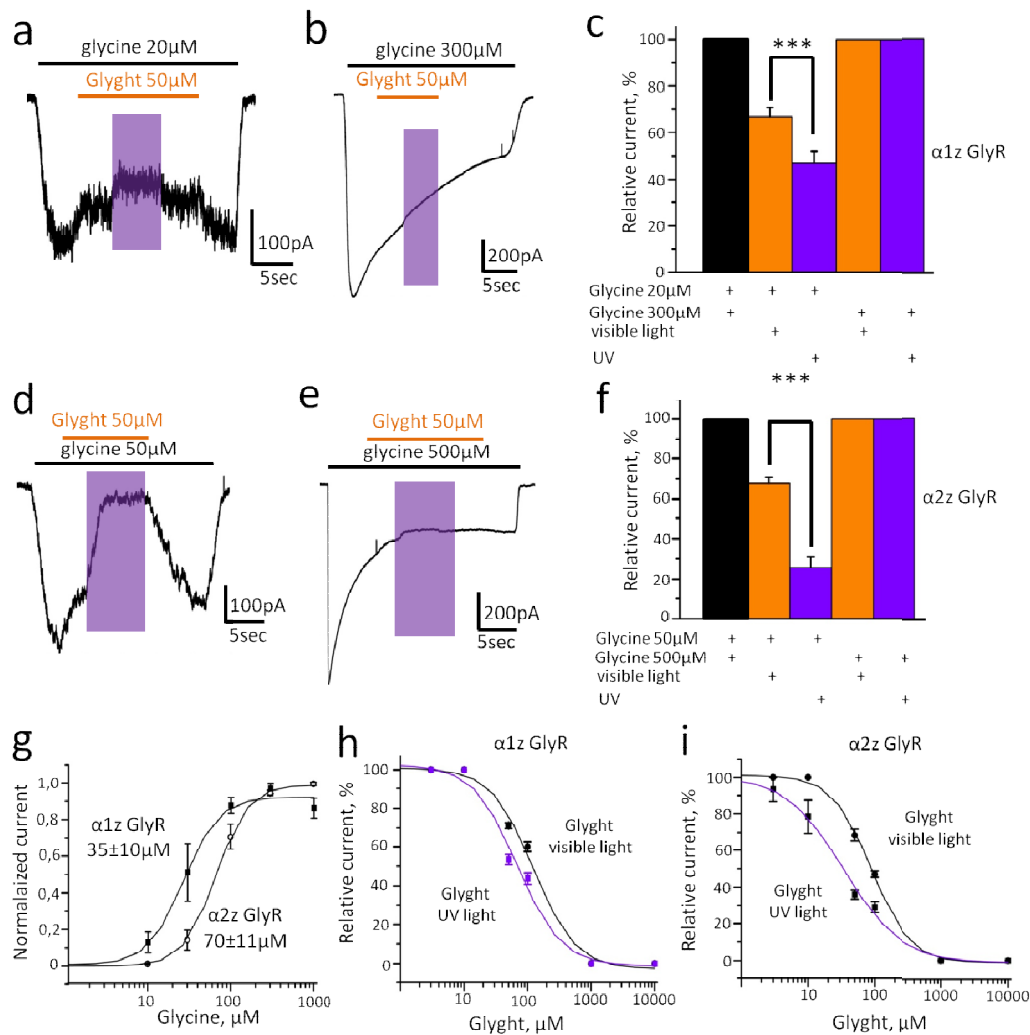
Larvae activity ($\text{mm} \cdot \text{min}^{-1}$) over all visible and UV light periods was integrated for Vehicle and Glyght treatments (23 larvae per drug treatment). One-way ANOVA with Sidak's multiple comparison test was conducted (p -value = 0.05). Error bars represent S.E.M. Glyght induced a significant increase in larvae activity (p -value < 0.0001) compared to control larvae under UV light, and non-significant (n.s.) differences were found in the same larvae for visible light dependent activities.

Supplementary Figure 4



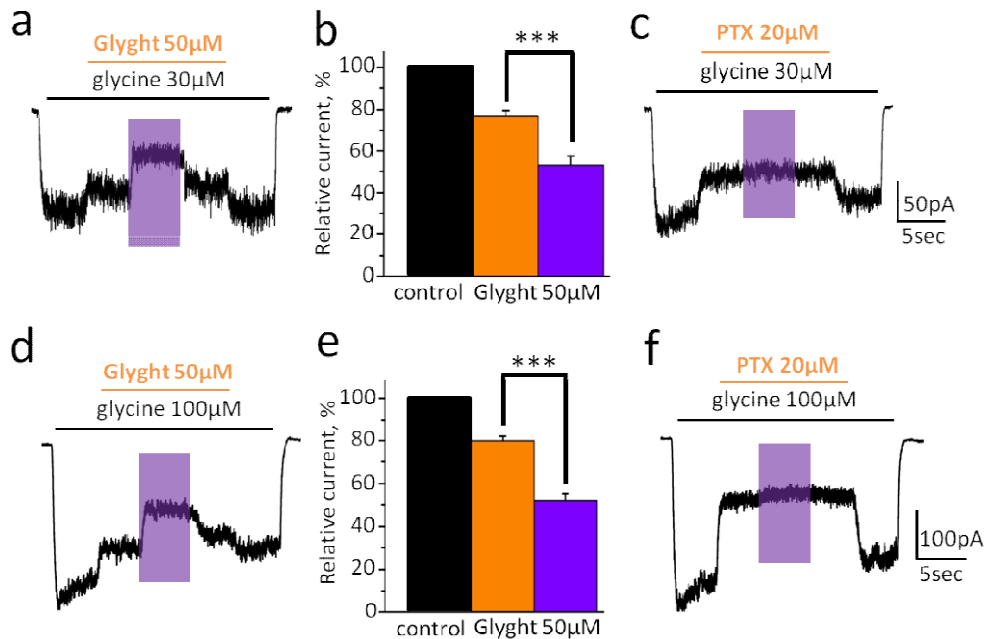
Glyght has only a minor inhibitory effect on GABA α R-mediated currents. Left: a representative recording of current induced by application of 5 μ M of GABA (black bar) and by mixture of GABA with Glyght 50 μ M (orange bar); UV illumination is indicated by violet rectangle. Right: a representative recording of current induced by application of 300 μ M of GABA and by mixture of GABA with Glyght 50 μ M; V_{hold} -30 mV.

Supplementary Figure 5



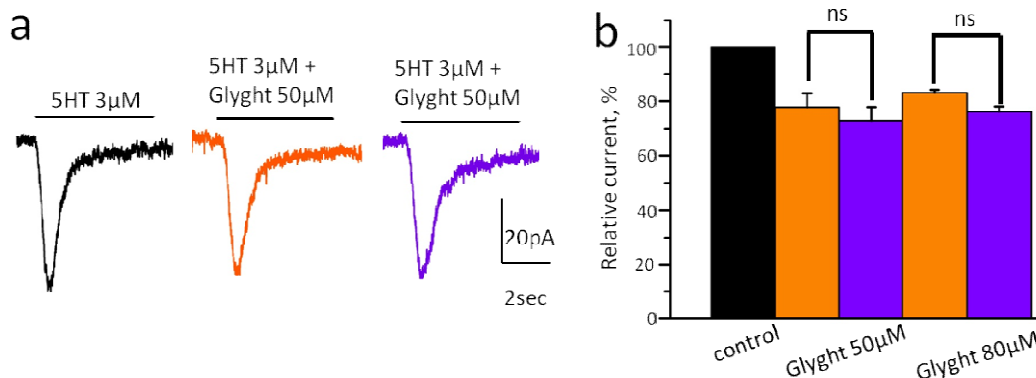
Glyht UV-dependently inhibits currents mediated by homomeric α 1Z and α 2Z GlyRs. **a**, Representative recording of the α 1Z-mediated current induced by application of glycine 20 μ M (indicated by black bar) and by mixture of glycine 20 μ M and Glyht 50 μ M (indicated by orange bar); time of UV illumination indicated by violet rectangle. **b**, Representative recording of the α 1Z current induced by 300 μ M of glycine and by mixture of glycine 300 μ M and Glyht 50 μ M. **c**, Relative amplitude of α 1Z currents in control (black column; 20 or 300 μ M of glycine were applied), at application of the mixture of glycine with Glyht 50 μ M under visible light (orange column) and mixture of glycine and Glyht 50 μ M under UV light (violet column), $p \leq 0.001$, $n = 8$. **d**, Representative trace of the α 2Z current induced by application of glycine 50 μ M and by mixture of glycine 50 μ M and Glyht 50 μ M. **e**, Representative recording of the α 2Z current induced by 500 μ M of glycine and by mixture of glycine 500 μ M and Glyht 50 μ M. **f**, Relative amplitude of α 2Z currents induced by application of glycine (50 or 500 μ M; black column), mixture of glycine with Glyht 50 μ M under visible light (orange column) and by mixture of glycine and Glyht 50 μ M under UV light (violet column), $p \leq 0.001$, $n = 4$. For all recordings $V_{\text{hold}} = -30$ mV. **g**, Cumulative dose/response curves for glycine at α 1Z (filled squares, $n = 6$) and α 2Z GlyRs (empty circles, $n = 6$). **h**, Cumulative dose/response curves for Glyht at α 1Z GlyRs at visible light (black curve) and upon UV illumination (violet curve); currents were induced by non-saturating concentration of glycine, $n = 5$. **i**, Cumulative dose/response curves for Glyht at α 2Z GlyRs at visible light (black curve) and under UV illumination (violet curve); currents were induced by non-saturating concentration of glycine, $n = 4$.

Supplementary Figure 6



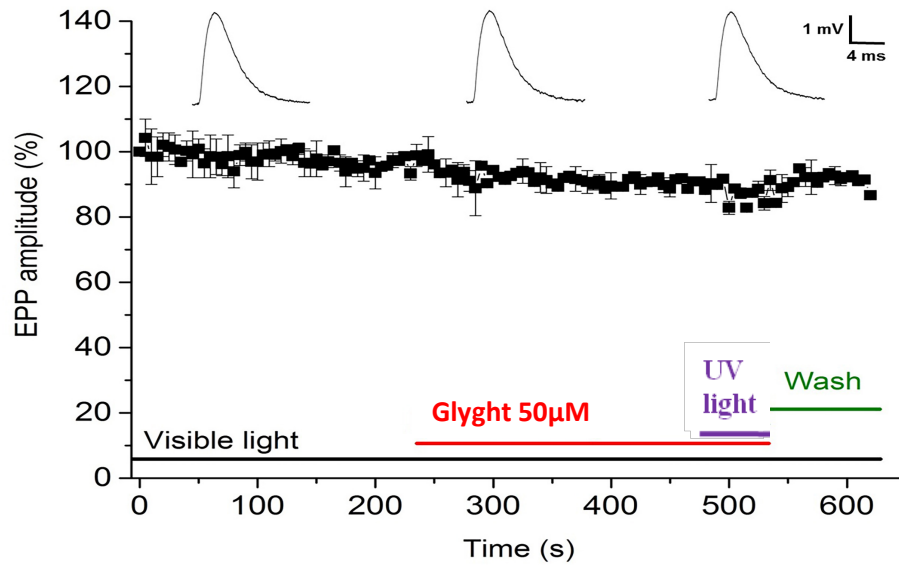
Glyght inhibited currents mediated by heteromeric $\alpha 1\beta$ and $\alpha 2\beta$ GlyRs in a UV-dependent manner. **a**, Representative recording of $\alpha 1\beta$ current induced by 30 μ M of glycine and by mixture of glycine 30 μ M/ Glyght 50 μ M at visible and UV light. **b**, Relative amplitude of $\alpha 1\beta$ currents in control (30 μ M of glycine; black column), at application of the mixture of glycine with Glyght 50 μ M under visible light (orange column) and mixture of glycine/ Glyght 50 μ M under UV light (violet column), $n = 7$, $p \leq 0.001$. **c**, Representative trace of $\alpha 1\beta$ current induced by glycine 30 μ M and by mixture of glycine with PTX 20 μ M, note the absence of the effect of UV light on the current amplitude. **d**, Representative recording of $\alpha 2\beta$ current induced by 100 μ M of glycine and by mixture of glycine 100 μ M / Glyght 50 μ M at visible and UV light. **e**, Relative amplitude of $\alpha 2\beta$ currents in control (100 μ M of glycine; black column), at application of the mixture of glycine with Glyght 50 μ M under visible light (orange column) and mixture of glycine/ Glyght 50 μ M under UV light (violet column), $n = 7$, $p \leq 0.001$. **f**, Representative trace of $\alpha 1\beta$ current induced by 100 μ M of glycine and by mixture of glycine with 20 μ M of PTX illustrating the absence of UV light effect on PTX induced inhibition.

Supplementary Figure 7



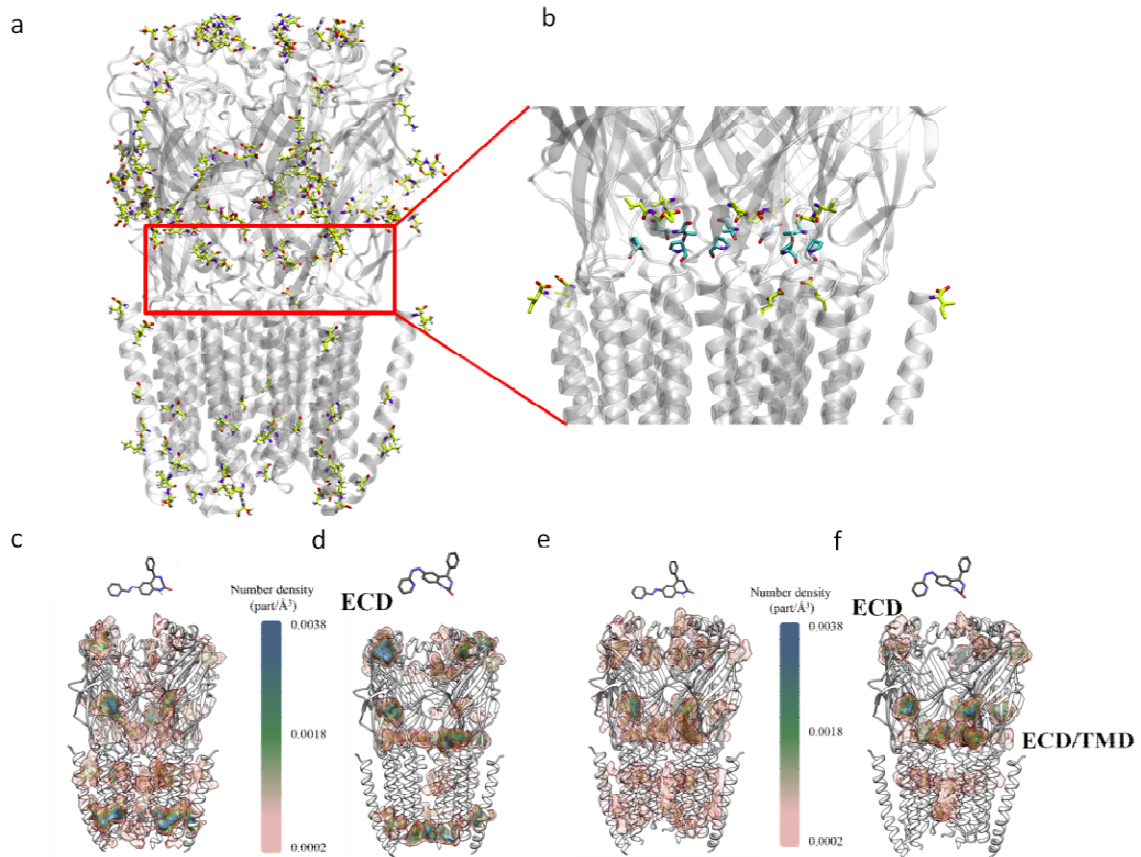
Glyght does not modulate the amplitude of currents mediated by 5HT_{3A} receptors. **a**, Representative traces of currents induced by application of 5HT 3 μ M (black trace), by mixture of 5HT with Glyght 50 μ M at visible light (orange trace) and by mixture of 5HT with Glyght 50 μ M at UV light (violet trace). **b**, Cumulative data on relative amplitude of 5HT-induced currents in control (black column), at application of 50 and 80 μ M of Glyght at visible light (orange columns) and at application of 50 and 80 μ M of Glyght at UV light (violet columns), $p > 0.05$, $n = 4$.

Supplementary Figure 8



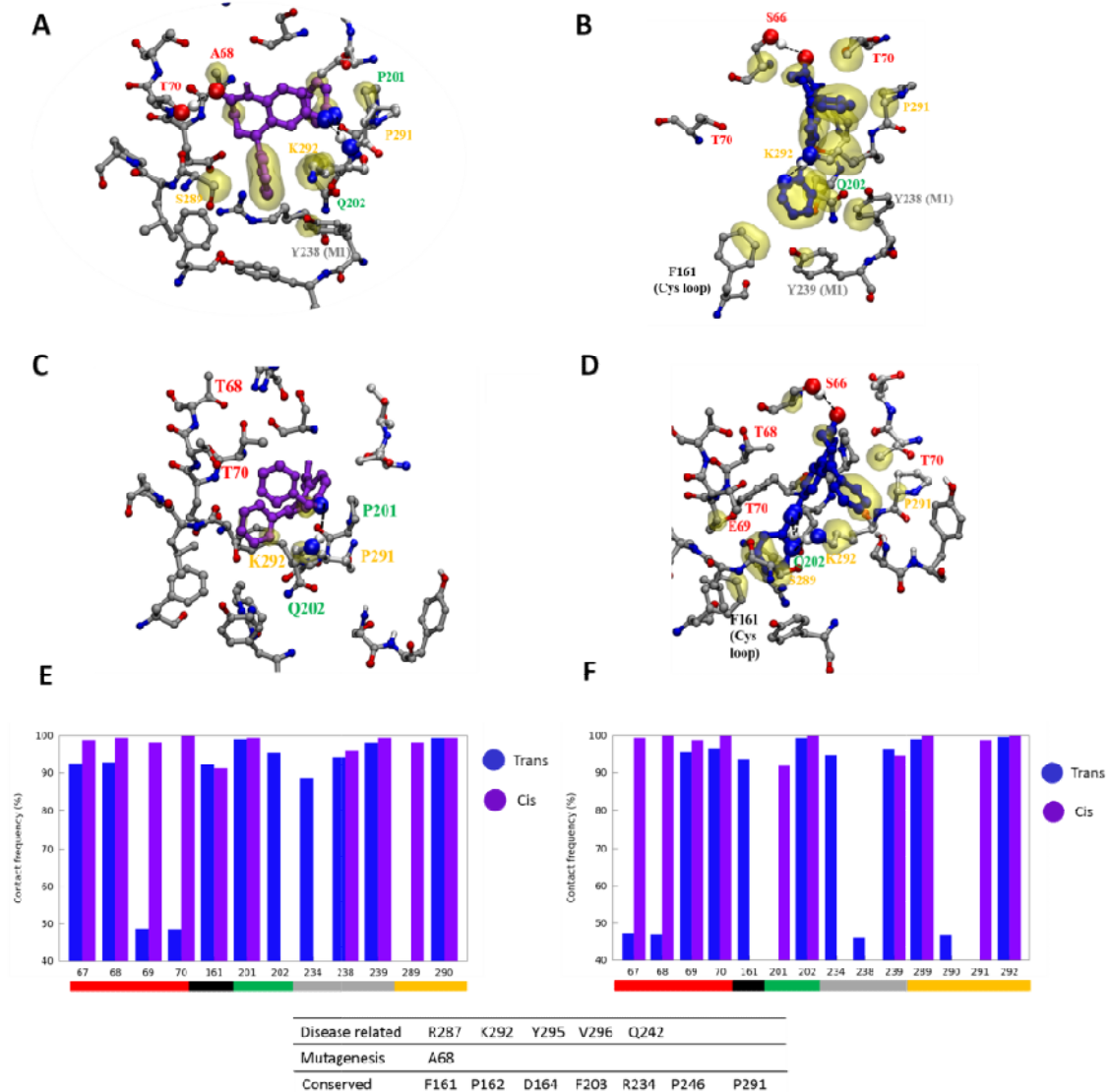
Testing the influence of Glyght on the amplitude of end-plate potentials at the neuromuscular junction. The effect of 100 μM of Glyght (shown by red line) on the amplitude of end-plate potentials (EPP) at the mouse neuromuscular junction when applied under the r light (shown by black line) and UV light (365 nm, shown by violet line). Glyght wash-out was done at the end of experiment (shown by green line). At the upper part of the figure are shown examples of native end-plate potential records at different moments of experiment: in control (left), during application of Glyght at visible light (middle) and at UV illumination (right).

Supplementary Figure 9



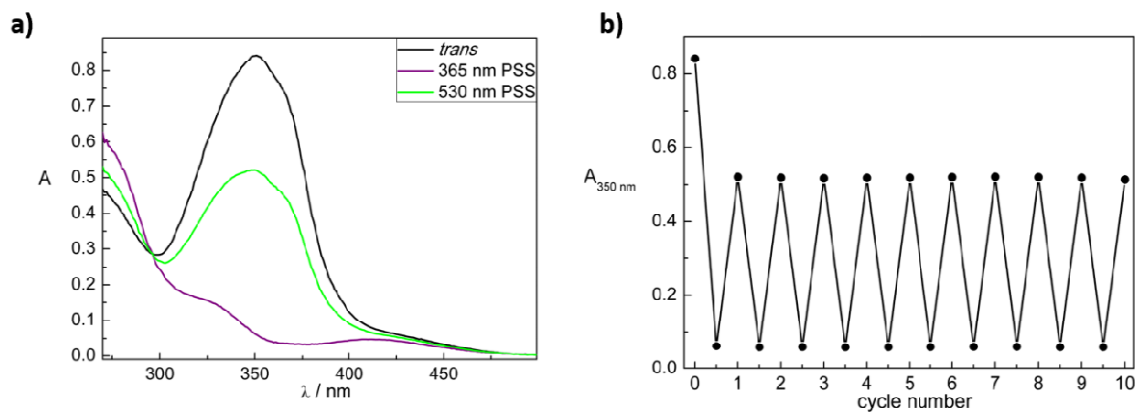
a, b. Density map of the ligand poses of Glyght obtained in the blind docking with the α_{1z} GlyR cryo-EM structure (Du *et al.*, 2015), which represents an open state. Each contour line corresponds to a number density of 0.0006 particles/ \AA^3 . **a,** *Trans* isomer (conformers M and P); **b,** *Cis* isomer (conformer M). For the sake of clarity, the front subunit is not shown. **c,d.** Density map of the ligand poses of Glyght obtained in the blind docking of the α_2 GlyR homology model (open state). Each contour line corresponds to a number density of 0.0006 particles/ \AA^3 . **c,** *Trans* isomer (conformers M and P); **d,** *Cis* isomer (conformer M). For the sake of clarity, the front subunit is not shown. **e,f.** ECD/TMD interface involved in the allosteric coupling between ligand binding to the ECD and opening of the ion channel pore in the TMD^{23–27}. Highly conserved amino acid residues throughout pGLICs²⁷, and residues whose mutation (either in natural variants or site-directed mutagenesis experiments) affect channel activation and conductance^{28,29} are shown in ball and sticks colored in white (C atoms), blue (N atoms) and red (O atoms).

Supplementary Figure 10



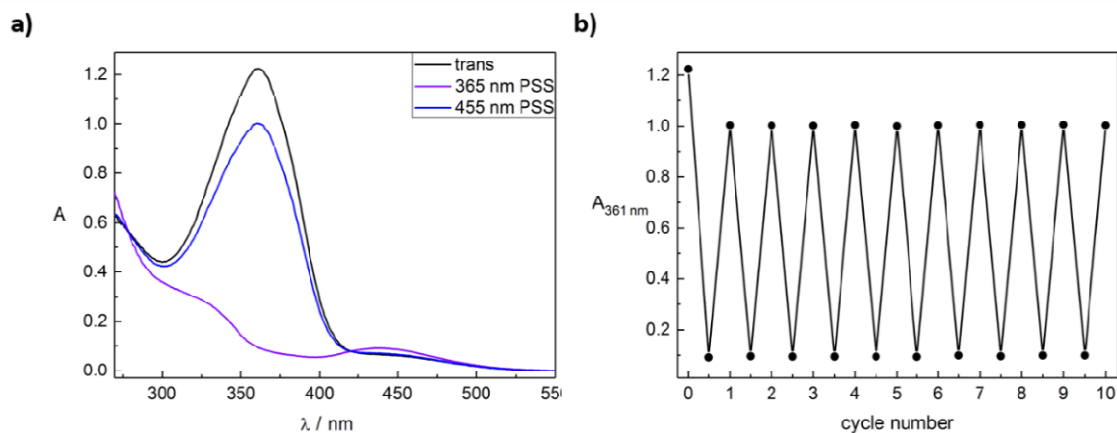
a, Detailed view of the most representative pose of *cis*-Glyht bound to the ECD/TMD interfacial site obtained in the flexible docking with α_1 GlyR. Hydrophobic contacts between *cis*-Glyht and the receptor residues are represented as a yellow surface and the atoms involved in hydrogen bonds between the ligand and Lys292 and Thr70 are represented with more voluminous balls and a dashed line. The residues in direct contact with *cis*-Glyht are indicated. **b, Detailed view of the most representative pose of *trans*-Glyht bound to the ECD/TMD interfacial site obtained in the flexible docking with α_1 GlyR.** Hydrophobic contacts between *trans*-Glyht and the receptor residues are represented as a yellow surface and the atoms involved in the hydrogen bonds between the ligand and Lys292 and Ser66 are represented with more voluminous balls and a dashed line. The residues in direct contact with *trans*-Glyht are indicated. **c, Detailed view of the *cis*-Glyht most probable binding site in α_2 GlyR (67-68IA \rightarrow 67-68 VT).** Hydrophobic contacts between *cis*-Glyht and the receptor residues are represented as a yellow surface and the atoms involved in the hydrogen bond between the ligand and Lys292 are represented with more voluminous balls and a dashed line. The residues in direct contact with *cis*-Glyht are indicated. **d, Detailed view of the *trans*-Glyht most probable binding site in α_2 GlyR.** Hydrophobic contacts between *trans*-Glyht and the receptor residues are represented as a yellow surface and the atoms involved in the hydrogen bonds between the ligand and Lys292, Gln202 and Ser66 are represented with more voluminous balls and a dashed line. The residues in direct contact with *trans*-Glyht are indicated. **e, Percentage of the frequency that a residue is closer than 5Å with Glyhtin α_1 GlyR.** In blue the *trans*-Glyht isomer and in violet, *cis*-Glyht. A coloured box below the residues numbers indicates to which loop they belong; red, black, green, grey and yellow correspond to β_1 - β_2 , Cys, β_8 - β_9 , preM1-M1 and M2-M3 loops, respectively. **f, Percentage of the frequency that a residue is closer than 5Å with Glyhtin α_2 GlyR.** In blue the *trans*-Glyht isomer and in violet, *cis*-Glyht. A coloured box below the residue numbers indicates to which loop they belong; the same colour code as in panel (e) is used. The highly conserved residues in the pGLICs family and the residues whose mutation affects negatively the channel activity and conductance^{9,28,29} are listed in the table below.

Supplementary Figure 11



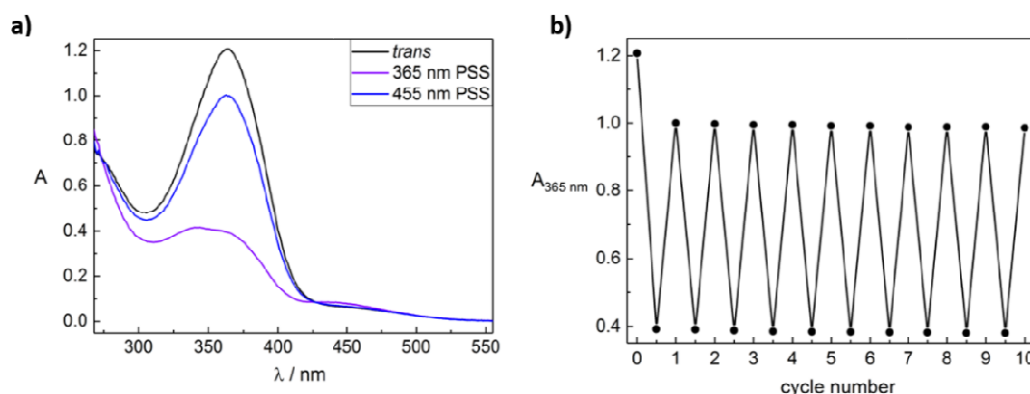
a, UV-Vis spectra of **3a** (50 μM in DMSO) from the *trans* isomer (black) at its thermal equilibrium, the PSS at illumination with UV-light of 365 nm (purple) and the PSS at illumination with blue light of 530 nm (green). **b**, Cycle performance of **3a** (50 μM in DMSO). Changes in absorption at 350 nm were measured during alternate illumination with light of 365 nm for 9 s and 530 nm for seven minutes.

Supplementary Figure 12



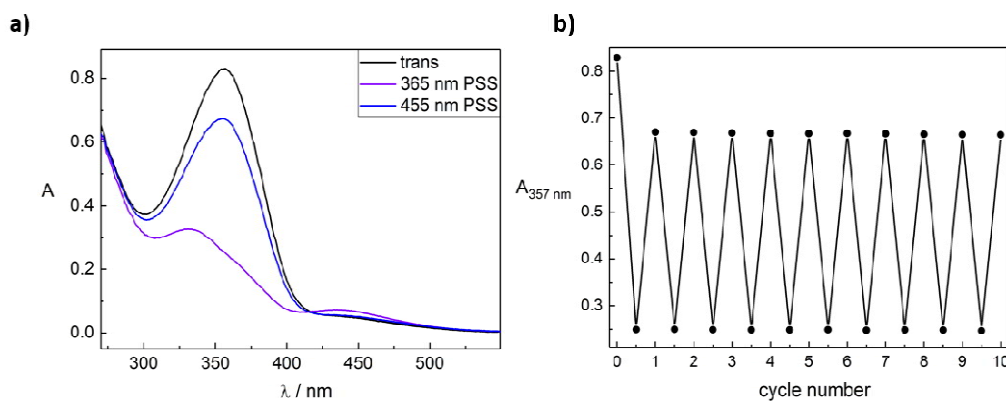
a, UV-Vis spectra of azo benzodiazepine **3b** (50 μM in DMSO) from the *trans* isomer (black), the PSS underillumination with UV-light of 365 nm (purple) and the PSS underillumination with blue light of 455 nm (blue). **b**, Cycle performance of azo benzodiazepine **3b** (50 μM in DMSO). Changes in absorption at 361 nm were measured during alternate illumination with light of 365 nm for 15 s and 455 nm for three seconds.

Supplementary Figure 13



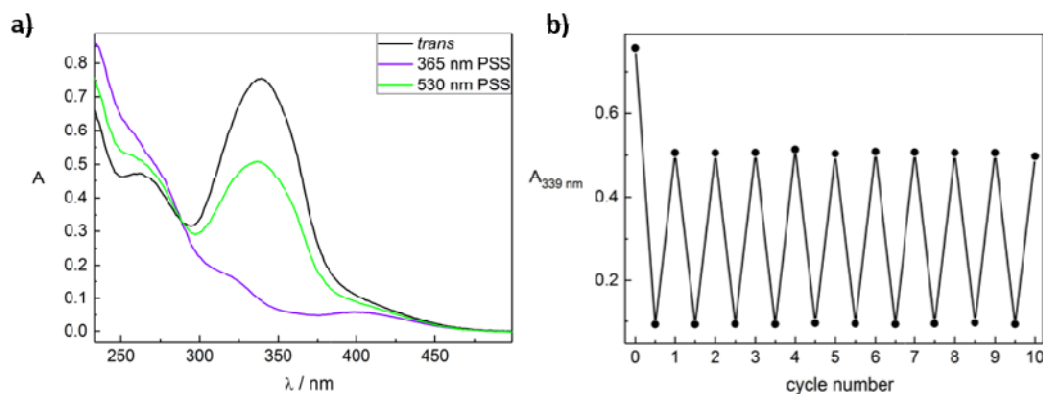
a, UV-Vis spectra of **3c** (50 μM in DMSO) from the *trans* isomer (black) at its thermal equilibrium, the PSS under illumination with UV-light of 365 nm (purple) and the PSS under illumination with blue light of 455 nm (blue). **b**, Cycle performance of **3c** (50 μM in DMSO). Changes in absorption at 365 nm were measured during alternate illumination with light of 365 nm and 455 nm.

Supplementary Figure 14



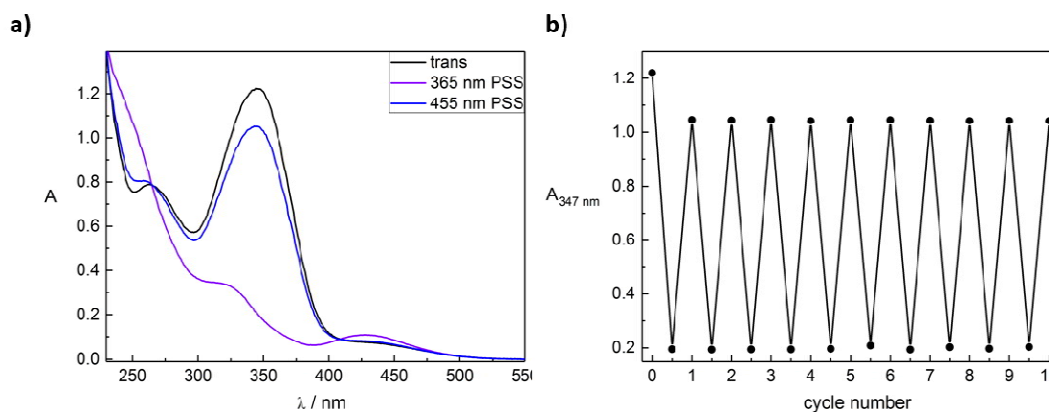
a, UV-Vis spectra of **3d** (50 μM in DMSO) from the *trans* isomer (black) at its thermal equilibrium, the PSS under illumination with UV-light of 365 nm (purple) and the PSS under illumination with blue light of 455 nm (blue). **b**, Cycle performance of **3d** (50 μM in DMSO). Changes in absorption at 357 nm were measured during alternate illumination with light of 365 nm for 15 s and 455 nm for three seconds.

Supplementary Figure 15



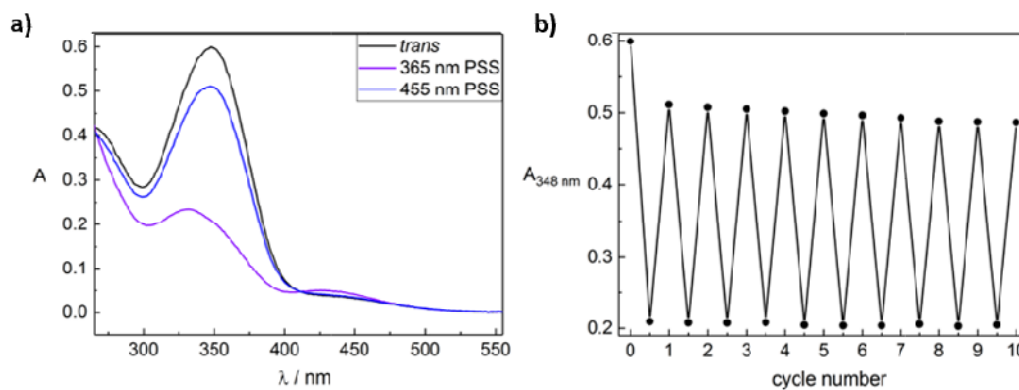
a, UV-Vis spectra of **3a**. (50 μM in PBS + 0.1% DMSO) from the *trans* isomer (black), the PSS under illumination with UV-light of 365nm (purple) and the PSS under illumination with blue light of 530nm (green). **b**, Cycle performance (50 μM in phosphate buffer + 0.1% DMSO). Changes in absorption at λ_{max} of the *trans* isomer were measured during alternate illumination with light of 365nm and 530 nm.

Supplementary Figure 16



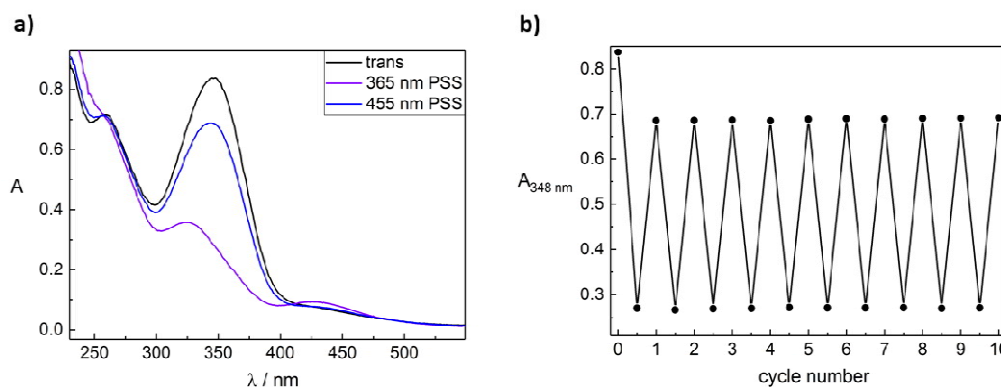
a, UV-Vis spectra azo benzodiazepine **3b** (50 μM in PBS + 0.1% DMSO) from the *trans* isomer (black), the PSS under illumination with UV-light of 365nm (purple) and the PSS under illumination with blue light of 455 nm (blue). **b**, Cycle performance of azo benzodiazepine **3b** (50 μM in phosphate buffer + 0.1% DMSO). Changes in absorption at λ_{max} of the *trans* isomer were measured during alternate illumination with light of 365 nm and 455 nm.

Supplementary Figure 17



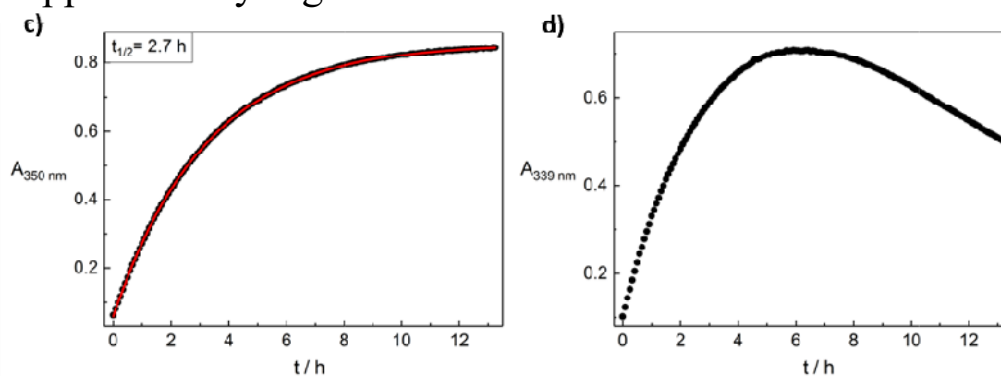
a, UV-Vis spectra of azo benzodiazepine **3c** (30 μM in PBS + 3% DMSO) from the *trans* isomer (black), the PSS under illumination with UV-light of 365 nm (purple) and the PSS under illumination with blue light of 455 nm (blue). **b**, Cycle performance (30 μM in phosphate buffer + 3% DMSO). Changes in absorption at λ_{max} of the *trans* isomer were measured during alternate illumination with light of 365 nm and 455 nm.

Supplementary Figure 18



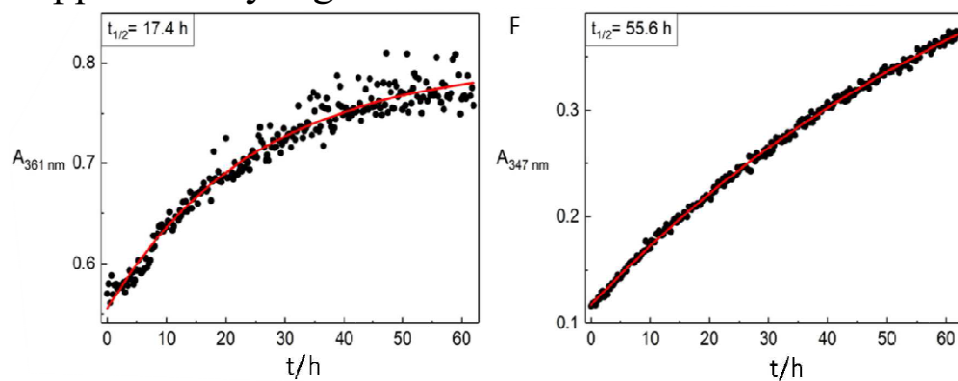
a, UV-Vis spectra of azo benzodiazepine **3d** (50 μM in PBS + 0.1% DMSO) from the *trans* isomer (black), the PSS under illumination with UV-light of 365 nm (purple) and the PSS under illumination with blue light of 455 nm (blue). **b**, Cycle performance (50 μM in phosphate buffer + 0.1% DMSO). Changes in absorption at λ_{max} of the *trans* isomer were measured during alternate illumination with light of 365 nm and 455 nm.

Supplementary Figure 19



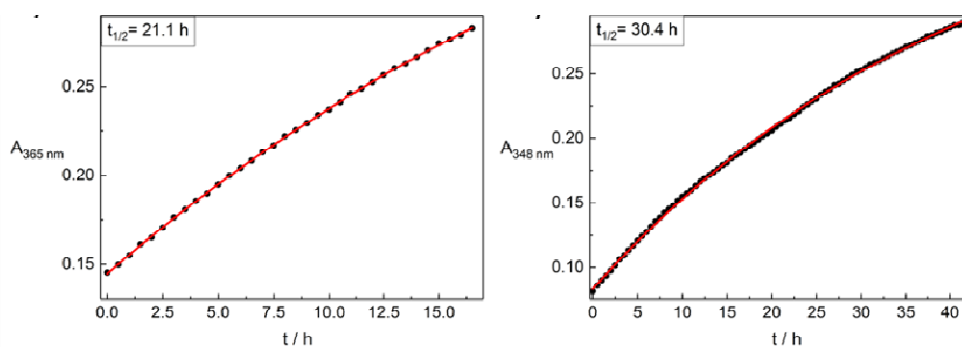
Compound 3a. Determination of the thermal half-lives at 25 °C. **Left:** 50 μM in DMSO. **Right:** 50 μM in phosphate buffer + 0.1% DMSO.

Supplementary Figure 20



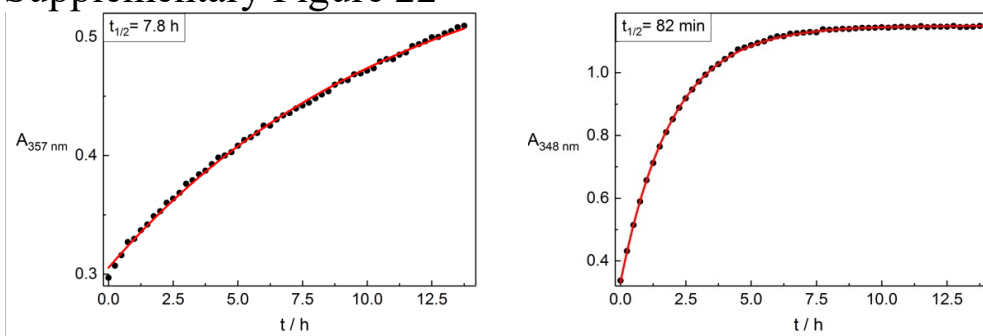
Compound 3b. Determination of the thermal half-lives at 25 °C. **Left:** 50 μM in DMSO. **Right:** 50 μM in phosphate buffer + 0.1% DMSO.

Supplementary Figure 21



Compound 3c. Determination of the thermal half-lives at 25 °C. **Left:** 50 μM in DMSO. **Right:** 50 μM in phosphate buffer + 0.1% DMSO.

Supplementary Figure 22



Compound 3d. Determination of the thermal half-lives at 25 °C. **Left:** 50 μM in DMSO. **Right:** 50 μM in phosphate buffer + 0.1% DMSO.

Supplementary Table 1

Photochemical properties of substituted azobenzene benzodiazepine derivatives **3 a-d**.

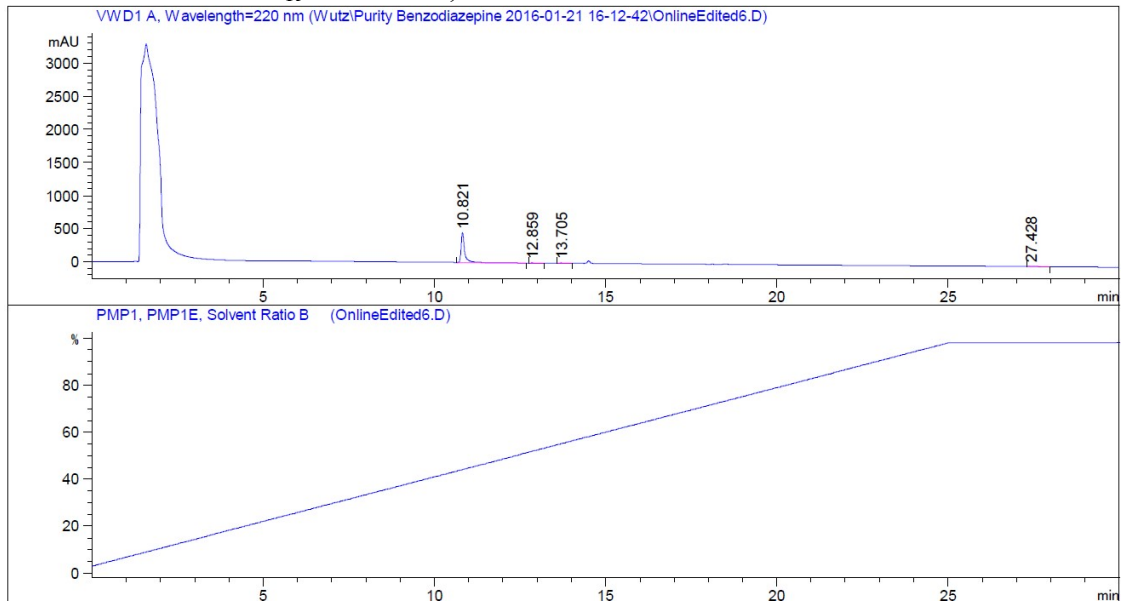
Entry	Cpd	Conc. [μ M]	solvent	λ_{\max}^{trans} [nm]	λ_{\max}^{cis} [nm]	$t_{1/2}(25^\circ\text{C})$ [h]	PSS ^[*,a] <i>cis</i> [%]	PSS ^[*,b] <i>trans</i> [%]
1	3a	50	DMSO	350	none	2.7 h	88	71
2	3a	50	PBS + 0.1% DMSO	339	none	- ^[c]	n.d.	n.d.
3	3b	50	DMSO	361	440	17.4	88	82
4	3b	50	PBS + 0.1% DMSO	347	429	55.6	n.d.	n.d.
5	3c	50	DMSO	365	442	21.1	88	82
6	3c	50	PBS + 0.1% DMSO	348	427	30.4	n.d.	n.d.
7	3d	50	DMSO	357	435	7.8	80	84
8	3d	50	PBS + 0.1% DMSO	348	425	1.4	n.d.	n.d.

n.d.: not determined; ^[*]determined by HPLC measurements; ^[a] PSS at photoconversion from the *trans* to the *cis* isomer; ^[b] PSS at photoconversion from the *cis* to the *trans* isomer. ^[c] could not be determined due to decomposition or precipitation after 5 h in PBS solution.

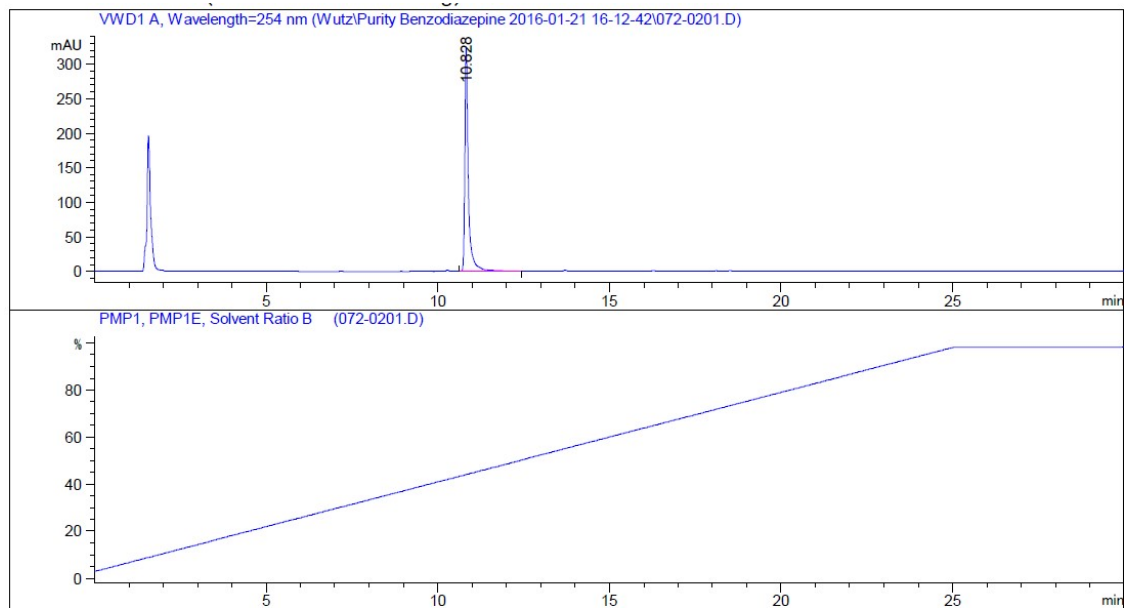
Analytical HPLC traces for Purity Determination

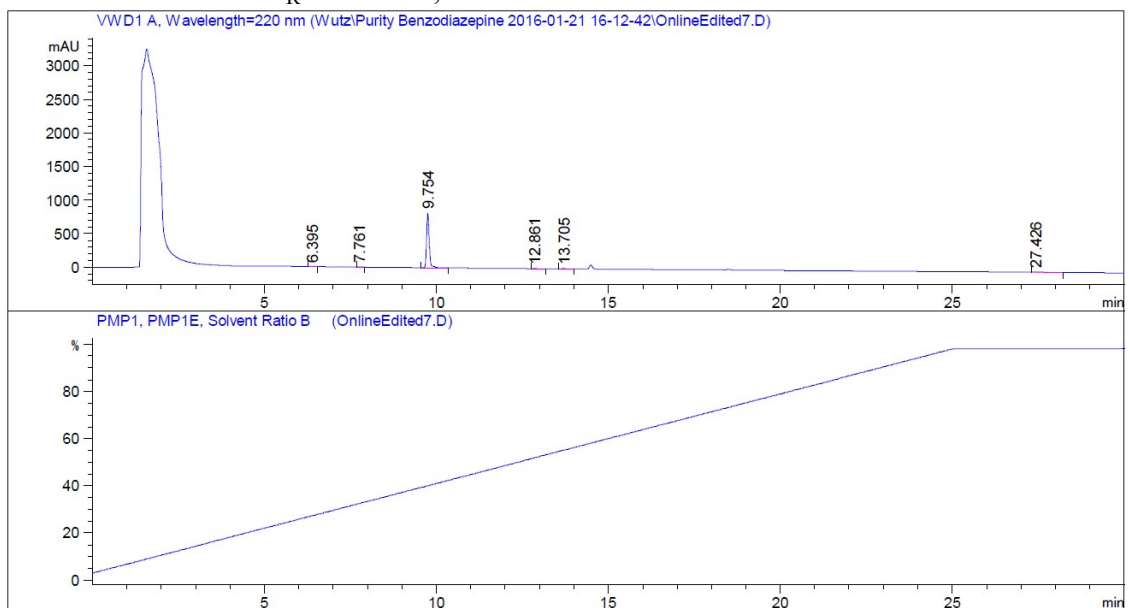
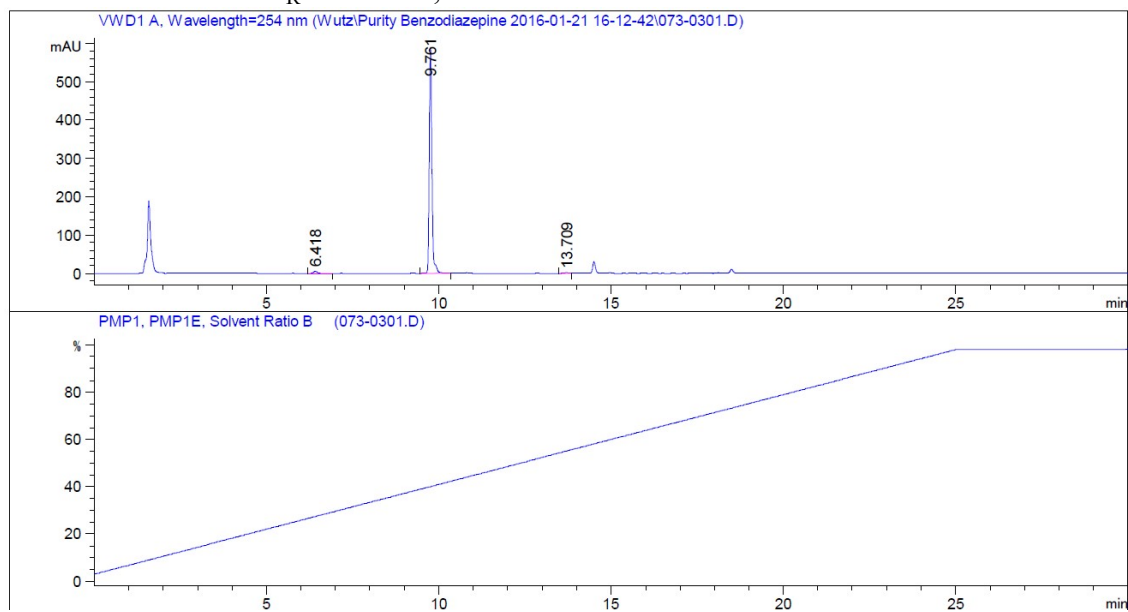
Compound 3a

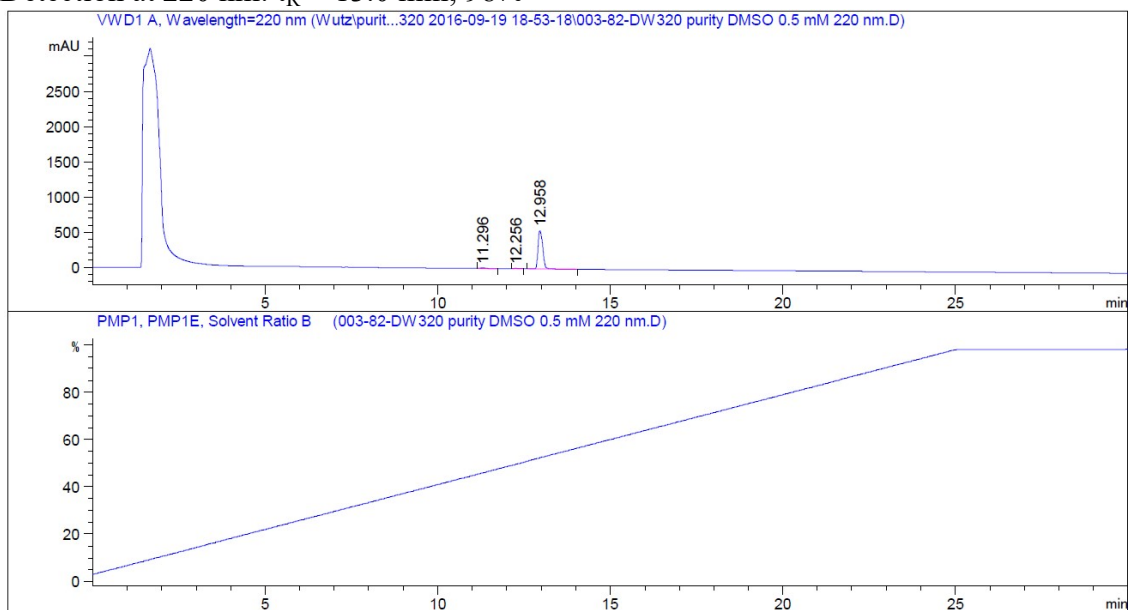
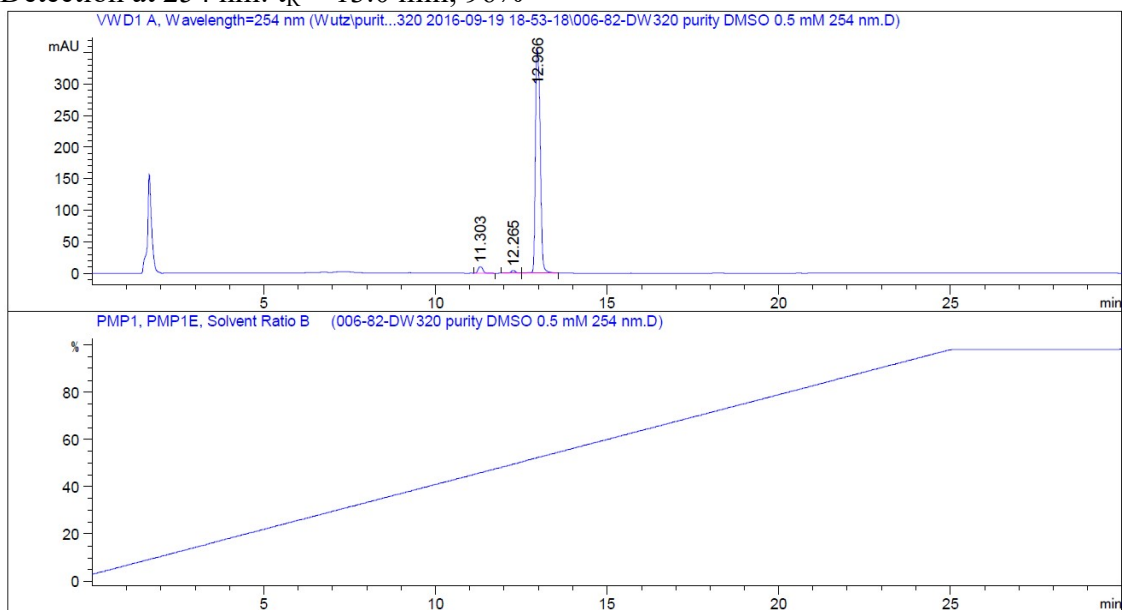
Detection at 220 nm: $t_R = 10.8$ min; 98%

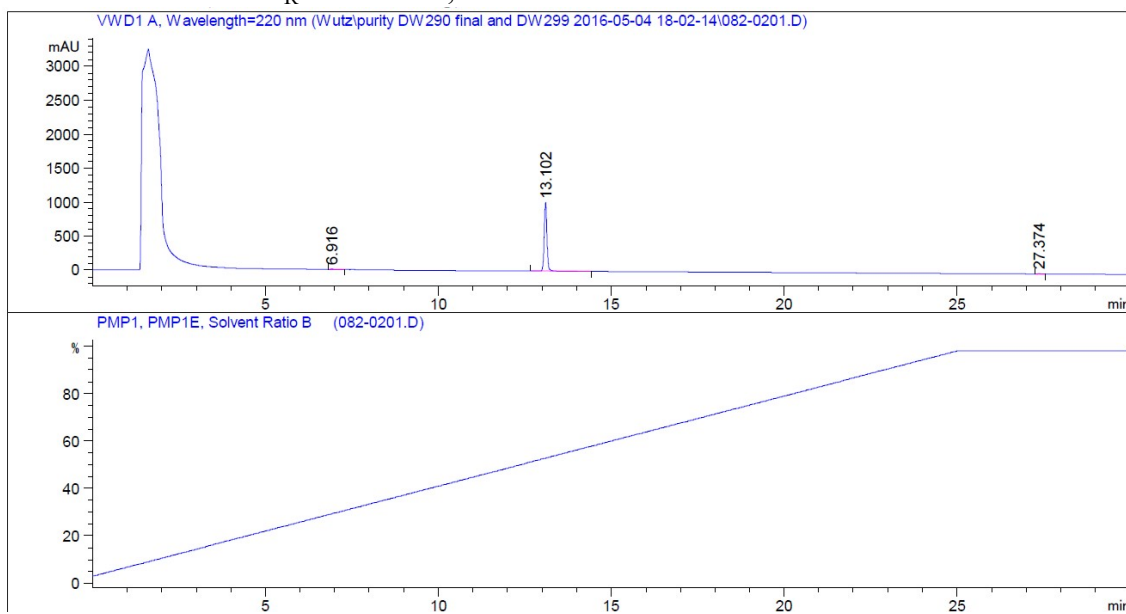
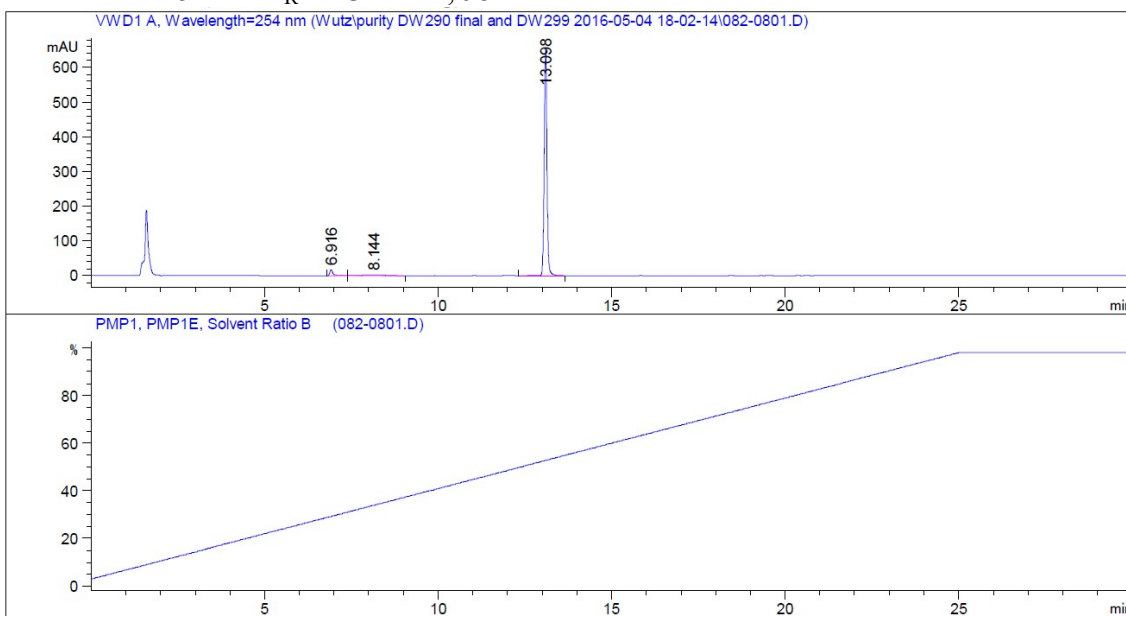


Detection at 254 nm: $t_R = 10.8$ min; 100%



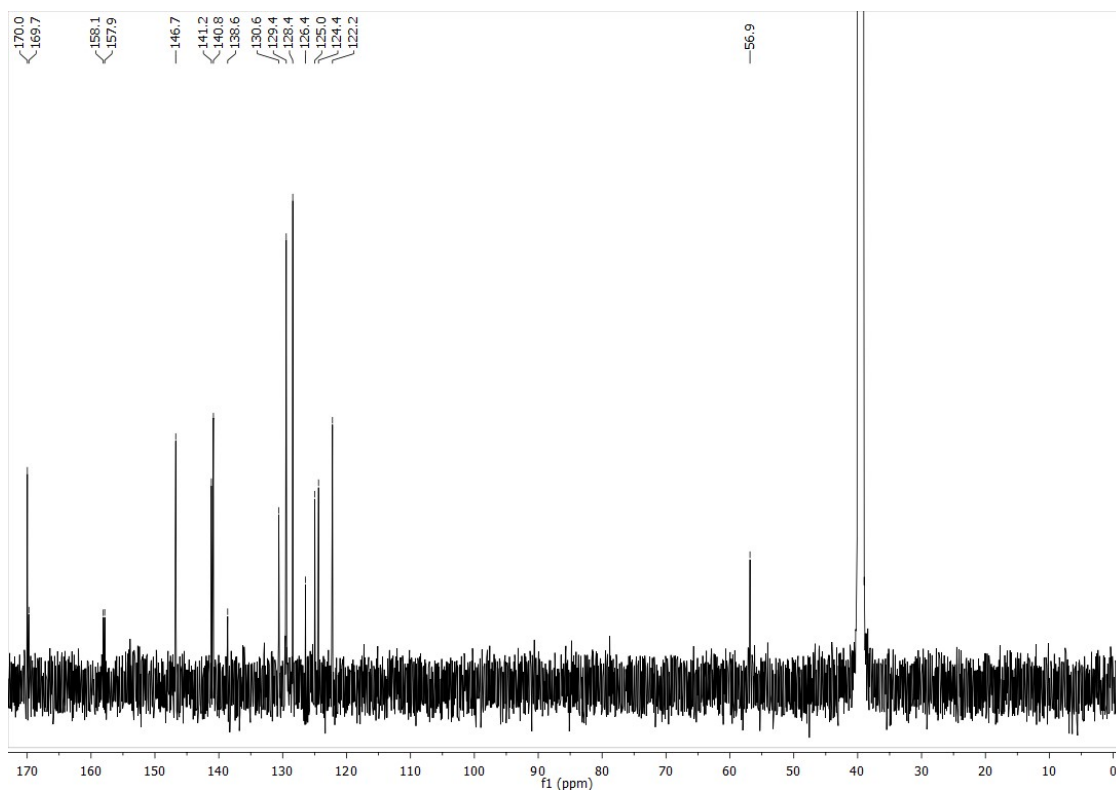
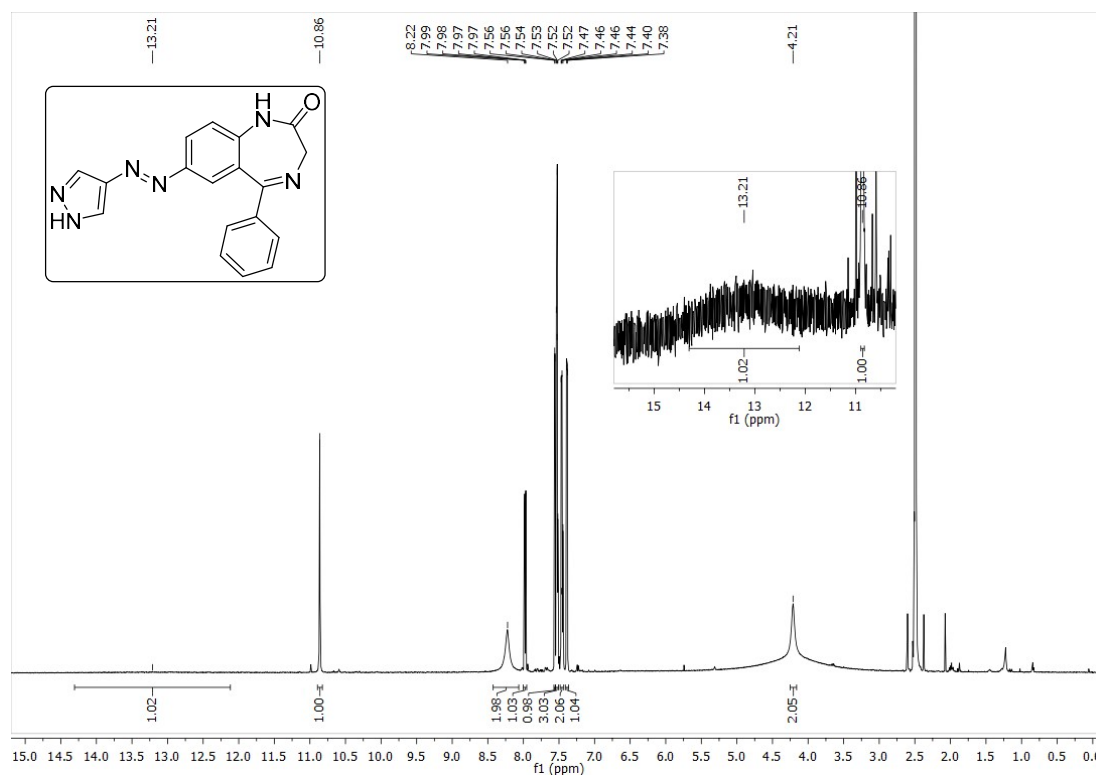
Compound 3bDetection at 220 nm: $t_R = 9.8$ min; 98%Detection at 254 nm: $t_R = 9.8$ min; 98%

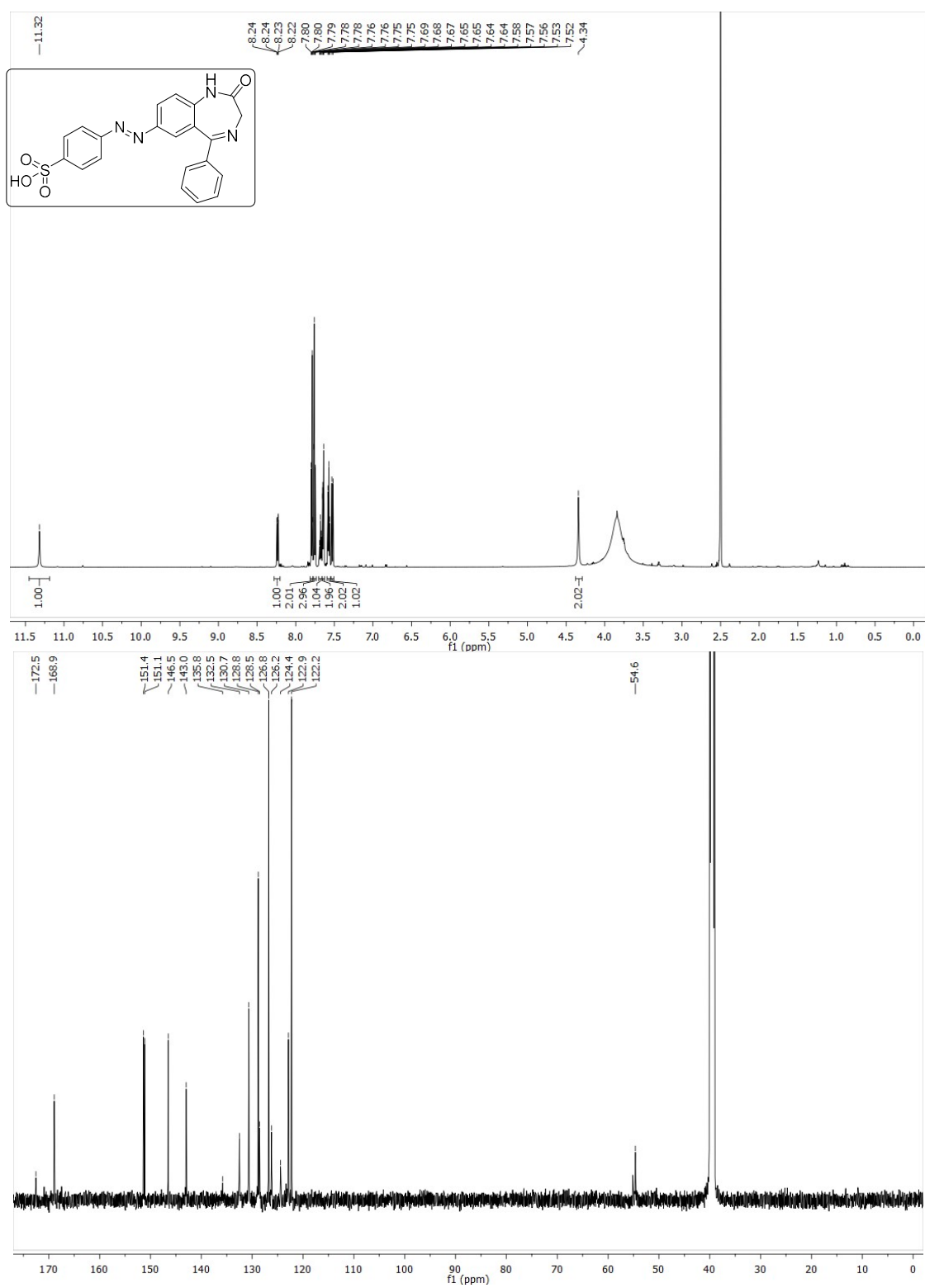
Compound **3c**Detection at 220 nm: $t_R = 13.0$ min; 98%Detection at 254 nm: $t_R = 13.0$ min; 96%

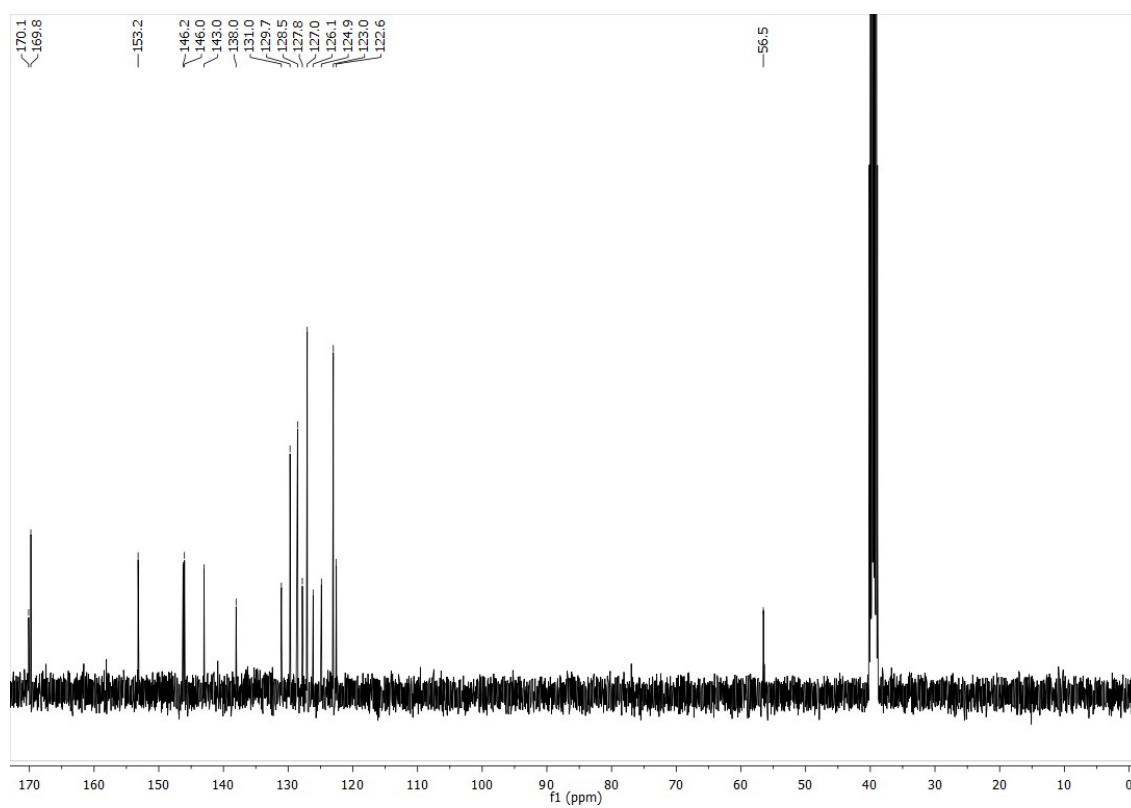
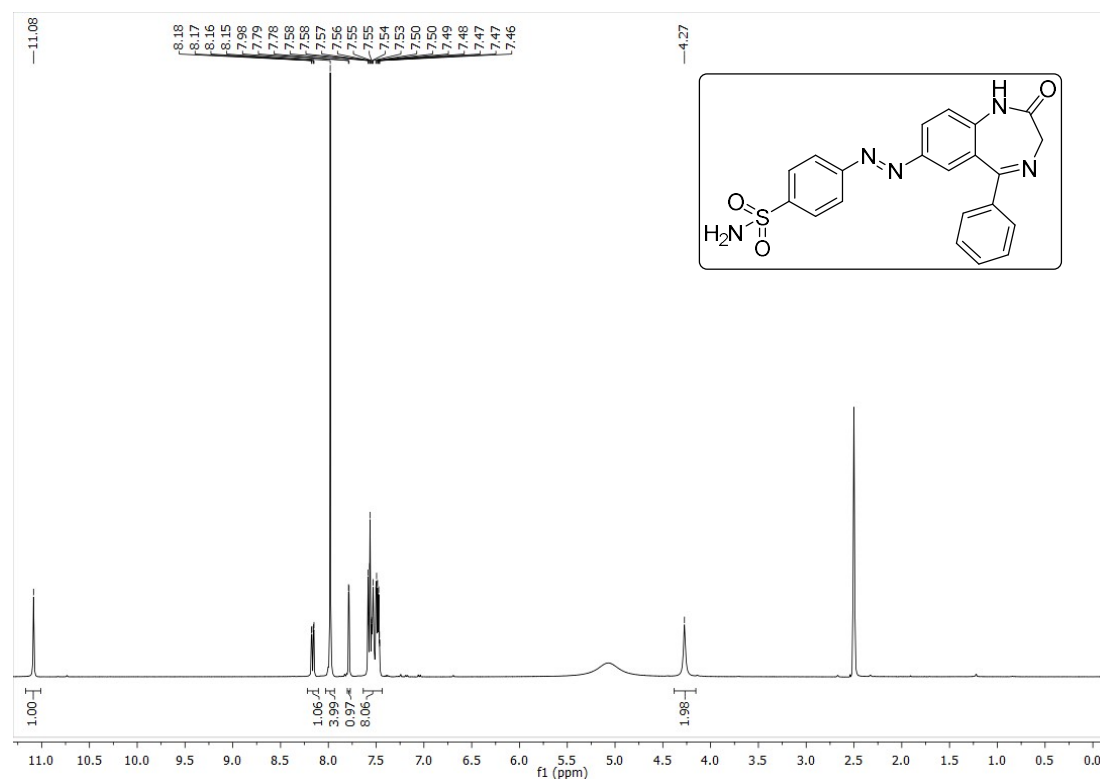
Compound 3dDetection at 220 nm: $t_R = 13.1$ min; 99%Detection at 254 nm: $t_R = 13.1$ min; 95%

^1H - and ^{13}C -NMR spectra

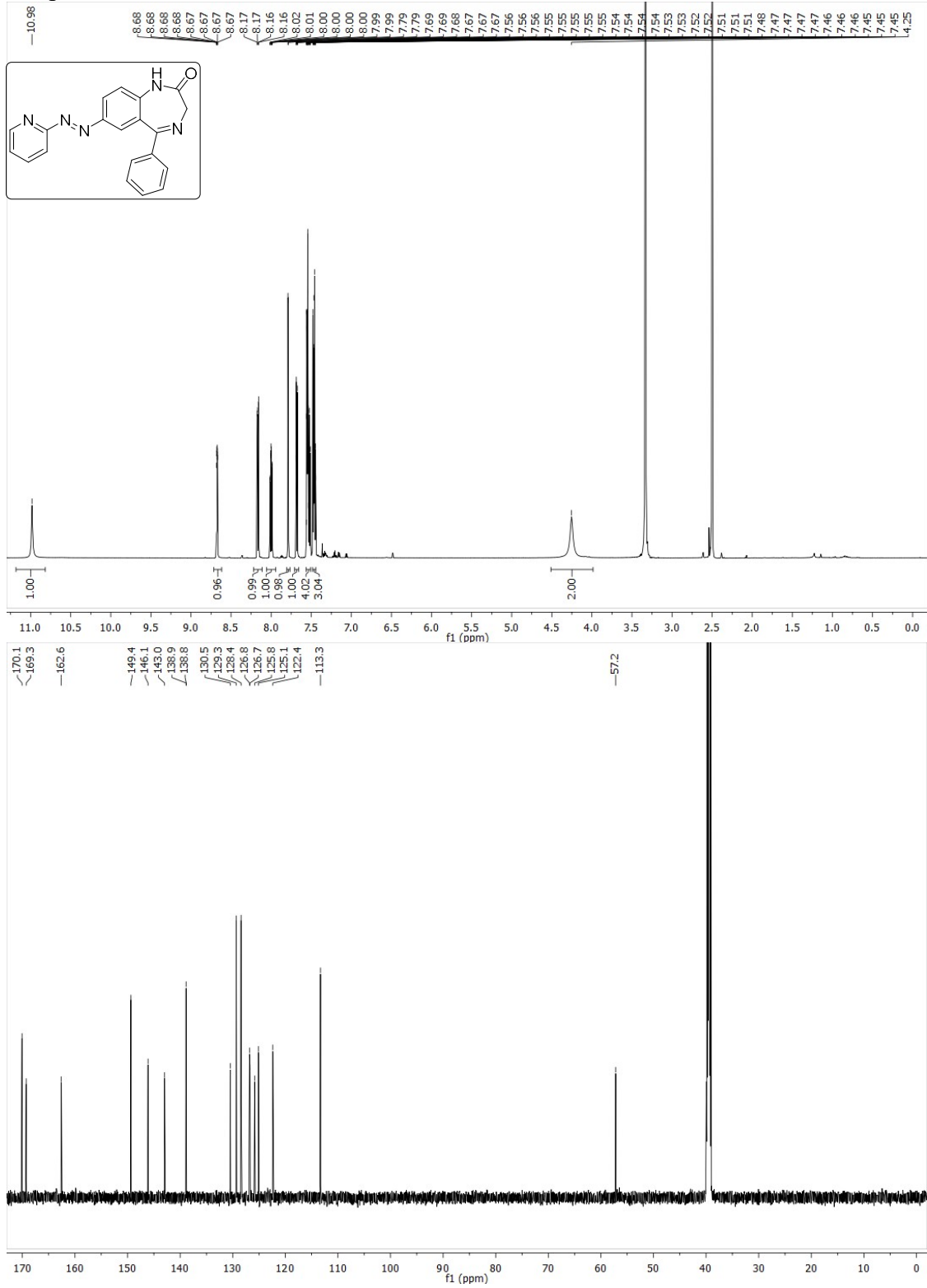
Compound 3a



Compound **3b**

Compound **3c**

Compound **3d**



1. Guandalini, L. *et al.* Design, synthesis and preliminary biological evaluation of new hydroxamate histone deacetylase inhibitors as potential antileukemic agents. *Bioorganic Med. Chem. Lett.* **18**, 5071–5074 (2008).
2. Severino, B. *et al.* Synthesis and pharmacological evaluation of peptide-mimetic protease-activated receptor-1 antagonists containing novel heterocyclic scaffolds. *Bioorganic Med. Chem.* **16**, 6009–6020 (2008).
3. Birkofer, L. & Franz, M. C-Nitrosierungen über Silyl-Derivate. *Chem. Ber.* (1971). doi:10.1002/cber.19711041009
4. Priewisch, B. & Rück-Braun, K. Efficient preparation of nitrosoarenes for the synthesis of azobenzenes. *J. Org. Chem.* (2005). doi:10.1021/jo048544x
5. Runtsch, L. S. *et al.* Azobenzene-based inhibitors of human carbonic anhydrase II. *Beilstein J. Org. Chem.* (2015). doi:10.3762/bjoc.11.127
6. Taylor, E. C., Tseng, C. P. & Rampal, J. B. Conversion of a Primary Amino Group into a Nitroso Group. Synthesis of Nitroso-Substituted Heterocycles. *J. Org. Chem.* (1982). doi:10.1021/jo00342a035
7. Mukhtarov, M. *et al.* Calibration and functional analysis of three genetically encoded Cl⁻/pH sensors. *Front. Mol. Neurosci.* **6**, 1–12 (2013).
8. Maleeva, G., Buldakova, S. & Bregestovski, P. Selective potentiation of alpha 1 glycine receptors by ginkgolic acid. *Front. Mol. Neurosci.* **8**, 1–11 (2015).
9. Du, J., Lü, W., Wu, S., Cheng, Y. & Gouaux, E. Glycine receptor mechanism elucidated by electron cryo-microscopy. *Nature* **526**, 224–9 (2015).
10. Justin Gullingsrud, Jan Saam, J. P. psfgen User's Guide. (2006).
11. Humphrey Dalke Schulten, W. A. K. Visual Molecular Dynamics. *Journal of Molecular Graphics* **14**, 33–38 (1996).
12. Hanwell, M. D. *et al.* Avogadro: An advanced semantic chemical editor, visualization, and analysis platform. *J. Cheminform.* (2012). doi:10.1186/1758-2946-4-17
13. Richter, L. *et al.* Diazepam-bound GABAA receptor models identify new benzodiazepine binding-site ligands. *Nat. Chem. Biol.* **8**, 455–464 (2012).
14. Rajagopal, A. K. & Callaway, J. Inhomogeneous electron gas. *Phys. Rev. B* (1973). doi:10.1103/PhysRevB.7.1912
15. Stephens, P. J., Devlin, F. J., Chabalowski, C. F. & Frisch, M. J. Ab Initio calculation of vibrational absorption and circular dichroism spectra using density functional force fields. *J. Phys. Chem.* **98**, 11623–11627 (1994).
16. Frisch, M. J. *et al.* Gaussian 09, Revision D.01. *Gaussian Inc.* 1–20 (2013). doi:10.1159/000348293
17. Trott, O. & Olson, A. Autodock vina: improving the speed and accuracy of docking. *J. Comput. Chem.* **31**, 455–461 (2010).
18. Raju, S. G., Barber, A. F., LeBard, D. N., Klein, M. L. & Carnevale, V. Exploring Volatile General Anesthetic Binding to a Closed Membrane-Bound Bacterial Voltage-Gated Sodium Channel via Computation. *PLoS Comput. Biol.* **9**, 1–10 (2013).
19. Bregestovski, P. D. & Maleeva, G. V. Photopharmacology: A Brief Review Using the Control of Potassium Channels as an Example. *Neurosci. Behav. Physiol.* **49**, 184–191 (2019).
20. Cohen, J., Arkhipov, A., Braun, R. & Schulten, K. Imaging the migration pathways for O₂, CO, NO, and Xe inside myoglobin. *Biophys. J.* **91**, 1844–1857 (2006).
21. Durrant, J. D. & McCammon, J. A. BINANA: A novel algorithm for ligand-binding characterization. *J. Mol. Graph. Model.* **29**, 888–893 (2011).

22. Pettersen, E. F. *et al.* UCSF Chimera--a visualization system for exploratory research and analysis. *J. Comput. Chem.* **25**, 1605–12 (2004).
23. Cederholm, J. M. E., Schofield, P. R. & Lewis, T. M. Gating mechanisms in Cys-loop receptors. *Eur. Biophys. J.* **39**, 37–49 (2009).
24. Bartos, M., Corradi, J. & Bouzat, C. Structural basis of activation of Cys-loop receptors: The extracellular-transmembrane interface as a coupling region. *Mol. Neurobiol.* **40**, 236–252 (2009).
25. Andersen, N., Corradi, J., Bartos, M., Sine, S. M. & Bouzat, C. Functional Relationships between Agonist Binding Sites and Coupling Regions of Homomeric Cys-Loop Receptors. *J. Neurosci.* **31**, 3662–3669 (2011).
26. Bertozzi, C., Zimmermann, I., Engeler, S., Hilf, R. J. C. & Dutzler, R. Signal Transduction at the Domain Interface of Prokaryotic Pentameric Ligand-Gated Ion Channels. *PLoS Biol.* **14**, 1–25 (2016).
27. Jaiteh, M., Taly, A. & Héning, J. Evolution of pentameric ligand-gated ion channels: Pro-loop receptors. *PLoS One* **11**, 1–24 (2016).
28. Lynch, J. W. *et al.* Identification of intracellular and extracellular domains mediating signal transduction in the inhibitory glycine receptor chloride channel. *EMBO J.* **16**, 110–120 (1997).
29. Ryan, S. G. *et al.* A missense mutation in the gene encoding the $\alpha 1$ subunit of the inhibitory glycine receptor in the spasmodic mouse. *Nat. Genet.* **7**, 131–135 (1994).